

Fakultät für  
Maschinenbau,  
Fahrzeugtechnik,  
Flugzeugtechnik



# Master's Thesis

## development of a manipulation system for the mini-RASSOR, suitable for basic additive manufacturing technologies

Bruckmoser, Jakob Matrikelnr. 29183316 \_\_\_\_\_

Supervisors:

Karl-Heinz Siebold, PhD

Department of Aeronautical Engineering, Hochschule München

Mike Conroy

Florida Space Institute, University of Central Florida

Munich, 16th March 2021

## Declaration of the editor

I hereby declare that I have done the editing independently and without outside help and that I have not used any sources or aids other than those indicated and that I have marked literal and analogous quotations as such.

---

Location, Date

---

Signature

## **Abstract**

This thesis covers the development of a 5 degrees of freedom manipulation system for the mini-RASSOR as part of the RE-RASSOR project. This manipulation system is able to place sintered Regolith pavers on the lunar surface to build a vertical takeoff, vertical landing pad to mitigate effects of lander rockets engine exhaust plumes. During the development a 3D printable cycloidal gear was created and tested.

# Contents

<b>List of Tables</b>	<b>5</b>
<b>List of Figures</b>	<b>7</b>
<b>Nomenclature</b>	<b>9</b>
<b>1 Introduction</b>	<b>10</b>
<b>2 Requirements</b>	<b>11</b>
2.1 Applicable Documents . . . . .	11
2.2 Means of Compliance . . . . .	11
2.3 Design Requirements . . . . .	11
2.4 General Requirements . . . . .	12
2.5 Mechanical Requirements . . . . .	13
<b>3 Robotic arms on Rovers and in space</b>	<b>15</b>
3.1 Robotic Arms . . . . .	15
3.2 Joint Connection Types and Cable Routing . . . . .	17
<b>4 Pre-Design</b>	<b>18</b>
4.1 Possible Designs . . . . .	18
4.2 Pre-Design Calculations . . . . .	19
4.2.1 Forward Kinematics . . . . .	19
4.2.2 Denavit-Hartenberg Method . . . . .	20
4.2.3 Geometric Approach . . . . .	21
4.2.4 Inverse Kinematics . . . . .	22
4.2.5 Geometric Method . . . . .	23
4.2.6 Quasi Numerical Method . . . . .	25
4.3 Design Selection . . . . .	28
4.4 First Static and Dynamic Analyses . . . . .	29
4.5 Second Iteration . . . . .	36
4.6 Section Analysis . . . . .	38
4.7 Third Iteration . . . . .	41
4.8 Final Iteration . . . . .	43
<b>5 Design</b>	<b>45</b>
5.1 Transmission . . . . .	45
5.1.1 Strain Wave Gear . . . . .	45
5.1.2 Design of the Strain Wave Gear . . . . .	45
5.1.3 Cycloidal Drive . . . . .	49
5.1.4 Design of the Cycloidal Drive . . . . .	50

---

5.2 Design of the Links of the Arm . . . . .	52
<b>6 Testing</b>	<b>55</b>
6.1 Material Properties of 3D printed PLA . . . . .	55
6.2 Software . . . . .	58
6.3 Propagation of uncertainty . . . . .	59
6.4 Transmission Tests . . . . .	60
6.5 Transmission Selection . . . . .	64
<b>7 Assembly</b>	<b>65</b>
7.1 Assembly of the Cycloidal Drive . . . . .	65
<b>Literature</b>	<b>67</b>
<b>Appendix</b>	<b>69</b>

## List of Tables

1	specifications of the used documents . . . . .	11
5	Properties of different Aerospace Mechanical Arms . . . . .	16
6	DH parameters for Design 1 . . . . .	20
7	Links length for Design 3 with minimal total length . . . . .	23
8	Links length for Design 4 with minimal total length . . . . .	24
9	Links length for Design 1 with minimal total length . . . . .	27
10	Design Comparison . . . . .	28
11	DH parameters for Design 3 . . . . .	29
12	Assumption of the masses . . . . .	31
13	Static results in the standard configuration. Forces in [N], Torques in [Nm] . . .	32
14	Static results in the stretched configuration. Forces in [N], Torques in [Nm] . . .	32
15	Dynamical results in the stretched configuration while stationary . . . . .	34
16	Dynamical results in the stretched configuration while decelerating . . . . .	34
17	Dynamical results in the standard configuration while decelerating . . . . .	34
18	Bending and Torsion moment distribution . . . . .	35
19	Bending and Torsion moments and Factors . . . . .	35
20	Link lengths for for the second iteration . . . . .	36
21	Second Iteration: stretched configuration, stationary . . . . .	37
22	Bending and Torsion moments and Factors . . . . .	37
23	Properties of PLA [11] . . . . .	38
24	2nd moment of area and section modulus for different cross section profiles . . .	38
25	Cross Section Areas I Beam . . . . .	39
26	Cross Section Areas Tube . . . . .	39
27	DH parameters with offsets . . . . .	41
28	Link lengths for for the third iteration . . . . .	41
29	Reduction of the joint torques . . . . .	42
30	Cross Section Areas Tube Profile for the third iteration . . . . .	42
31	Increase of the joint torques . . . . .	43
32	Cross Section Areas Tube Profile for the final iteration . . . . .	43
33	Permissible moment load, stationary . . . . .	44
34	Permissible moment load, dynamic/decelerating . . . . .	44
35	Considered Motors for Transmission Calculation [16] . . . . .	46
36	Strain Wave Parameters for each Motor . . . . .	46
37	Torsion Test Results . . . . .	55
38	Serial Commands to control the Stepper Motor . . . . .	58
39	Propagation of uncertainty . . . . .	59
40	Torque Results of the Motor (17HS4401, ref. Appendix A) . . . . .	61
41	Transmission Tests for the Timing Belt Design . . . . .	61
42	Transmission Test for the TPU Design . . . . .	62

---

43	Transmission Tests for Cycloidal Drive (30:1) . . . . .	63
44	Transmission Tests for Cycloidal Drive (43:1) . . . . .	63
45	Summary of design types . . . . .	63
46	Bill of Material for Cycloidal Drive (43:1) . . . . .	66

## List of Figures

1	Different Aerospace Robotic Arms . . . . .	16
2	Mechanical solution, cable routing and comparison of the joint connection types [6] . . . . .	17
3	Different Designs for the manipulation system . . . . .	18
4	required points for the design to reach . . . . .	19
5	Coordinate Frames Design 1 for DH Parameters . . . . .	20
6	Kinematic Structure of Design 3 . . . . .	22
7	non linear optimization solver in <i>MATLAB</i> . . . . .	23
8	Result of the Length Optimization Design 3 . . . . .	24
9	Result of the Length Optimization Design 4 . . . . .	25
10	workspace as point cloud . . . . .	26
11	hull around workspace . . . . .	26
12	intersection check . . . . .	26
13	Result of the Length Optimization Design 1 . . . . .	27
14	Coordinate Frames Design 3 for DH Parameters . . . . .	29
15	Forces and moments acting on link i [10] . . . . .	30
16	Dummy paver for arm calculations . . . . .	36
17	Critical Buckling force [12] . . . . .	39
18	Moment/Force Progression over the length of link 2 and 3 . . . . .	40
19	Cross Sections for different Profiles . . . . .	40
20	Coordinate Frames with offsets for DH Parameters . . . . .	41
21	Unloading Sequence with Standard Configuration . . . . .	42
22	First draft designs of the different transmission designs . . . . .	47
23	All printed PLA Strain Wave Gear . . . . .	47
24	All printed TPU Strain Wave Gear . . . . .	48
25	Strain Wave Gear with Timing Belt . . . . .	48
26	Ordinary cycloidal Drive (left). Cycloidal drive with contracted cycloid disc (right) [17] . . . . .	49
27	Cycloidal Drive . . . . .	50
28	Explosion view of the Cycloidal Drive . . . . .	50
29	Eccentric Shaft design change . . . . .	51
30	Attachment Part Design . . . . .	52
31	Link 1 Design . . . . .	52
32	Link 2 and 3 Design . . . . .	52
33	Link 4/5 Design . . . . .	53
34	End Effector Design . . . . .	53
35	Complete Arm Design . . . . .	54
36	Test Setup for Torsion PLA Test . . . . .	55
37	Pictures of Torsion Test specimen Black PLA . . . . .	56

---

38	Pictures of Torsion Test specimen Yellow PLA . . . . .	57
39	First test setup for the Torque and Transmission Test . . . . .	60
40	Adapted Torque Test setup . . . . .	62
41	Required transmission ratios for each joint . . . . .	64
42	Cycloidal Drive Assembly . . . . .	65

# Nomenclature

## abbreviations

DH	Denavit-Hartenberg
DOF	Degree(s) of Freedom
FSI	Florida Space Institute
ISRU	In-situ resource utilization
PLA	Polyactide acid
RASSOR	Regolith Advanced Surface Systems Operations Robot
TPU	Thermoplastic polyurethane
UCF	University of Central Florida
VTVL	vertical takeoff, vertical landing

## symbols

$F$	Force	[N]
$M$	Moment	[Nm]
$r$	Transmission ratio	[–]

## indices

$b$	Force/Moment resulting in bending stress
$t$	Force/Moment resulting in torsional stress

# 1 Introduction

In-situ resource utilization (ISRU) is the practice of collecting and processing materials found on other astronomical objects like the moon. ISRU eliminates the need to deliver these materials from the earth and drastically decreases the payload weight and therefore the costs time of the project. According to NASA in-situ resource utilization “will enable the affordable establishment of extraterrestrial exploration and operations”<sup>1</sup>.

With the Regolith Advanced Surface Systems Operations Robot (RASSOR) NASA plans to mine the Regolith and create sintered Regolith Pavers. The pavers are used to create a platform for spacecrafts to land on in order to “mitigate the effects of a lander rocket engine exhaust plume impinging on the regolith surface, which can cause cratering and high speed ejecta” [1]. Florida Space Institute’s RE-RASSOR project (Research and Education version of the NASA RASSOR Robot) aims to create a rover mobility platform suitable for basic additive manufacturing technologies which is licensed for Research and Education use<sup>2</sup>.

This thesis covers the development of a 5 Degrees of Freedom manipulation system for the mini-RASSOR, which is able to place NASA Swampworks’ pavers onto the lunar surface, creating the vertical takeoff, vertical landing (VTOL) pad. It is settled in the FSI’s RE-RASSOR project, meaning that it is suited for basic additive manufacturing technologies. The main focus lies on the 3D printability of the design which resulted in the development of a 3D printable cycloidal drive.

---

<sup>1</sup>NASA - In-Situ Resource Utilization: [https://www.nasa.gov/centers/ames/research/technology-onepagers/in-situ\\_resource\\_Utiliza14.html](https://www.nasa.gov/centers/ames/research/technology-onepagers/in-situ_resource_Utiliza14.html) (accessed: 25.02.2020)

<sup>2</sup>Robotics - Florida Space Institute: <https://fsi.ucf.edu/robotics-2/> (accessed: 25.02.2020)

## 2 Requirements

### 2.1 Applicable Documents

Reference ID	Document ID	Document Name
AD - 01	MIL-HDBK-5J	Metallic materials and elements for aerospace vehicle structures
AD - 02	ECSS-E-ST-33-01C Rev.1	Space Engineering - Mechanisms
AD - 03	ECSS-E-ST-32C Rev.1	Space Engineering - Structural general requirements
AD - 04	ECSS-E-ST-32-10C Rev.1	Space Engineering - Structural factors of safety for spaceflight hardware

Table 1: specifications of the used documents

### 2.2 Means of Compliance

0 = General establishments, declarations, definitions	5 = Ground test
1 = Drawings, plans, descriptions, lists	6 = Flight test
2 = Calculations	7 = Inspections
3 = Safety analyses, error analyses	8 = Simulations
4 = Laboratory tests	9 = Equipment- / Device qualification
NC non compliant   C compliant   C* compliant with restrictions	

The requirements were taken from the ECSS standards for space mission designs, as this arm is planned to operate on the moon at some point. This thesis only creates an initial design which is meant to operate on the earth to show a proof of concept. The ECSS standards requirement were therefore soften so this specific project needs (e.g. no thermal vacuum conditions, no thermal control) and are not compliant with the ECSS standards.

### 2.3 Design Requirements

Req. ID	R_D 1				
Req. Name	Main objective				
Description	The arm shall be able to unload and place pavers onto a defined spot on the lunar surface.				
References	User	Moc	0	Compliance	C

Req. ID	R_D 2				
Req. Name	Lifting Force				
Description	The arm shall be able to lift the dedicated paver stone in lunar gravity				
References	User	Moc	0, 2	Compliance	C

<b>Req. ID</b>	R_D 3				
<b>Req. Name</b>	Manufacturing				
<b>Description</b>	The arm shall be designed for additive manufacturing.				
<b>References</b>	User	Moc	0, 4	<b>Compliance</b>	C

<b>Req. ID</b>	R_D 4				
<b>Req. Name</b>	Pavers Platform				
<b>Description</b>	The rover shall have a platform to transport at least two pavers.				
<b>References</b>	User	Moc	0	<b>Compliance</b>	C

<b>Req. ID</b>	R_D 5				
<b>Req. Name</b>	Deliverables				
<b>Description</b>	The final deliverables are the .stl-Files and the proprietary files of the design software (Fusion 360)				
<b>References</b>	User	Moc	0	<b>Compliance</b>	C

## 2.4 General Requirements

<b>Req. ID</b>	R_G 1				
<b>Req. Name</b>	Units				
<b>Description</b>	SI-units and associated symbols system shall be used.				
<b>References</b>	[AD-02] Chpt. 4.2.3	Moc	0	<b>Compliance</b>	C

<b>Req. ID</b>	R_G 2				
<b>Req. Name</b>	Redundancy				
<b>Description</b>	<p>During the design of the mechanism, all single point failure modes shall be identified.</p> <p>Failure of one element or part shall not prevent its redundant counterpart from performing its intended function or the mechanism from meeting its performance requirements.</p> <p>All single points of failure should be eliminated by redundant components.</p>				
<b>References</b>	[AD-02] Chpt. 4.2.5.1	Moc	2, 3, 4	<b>Compliance</b>	

<b>Req. ID</b>	R_G 3				
<b>Req. Name</b>	Reliability				
<b>Description</b>	Failure of one part or element shall not result in consequential damage to the equipment or other spacecraft components.				
<b>References</b>	[AD-02] Chpt. 4.2.5.1	Moc	3	<b>Compliance</b>	

<b>Req. ID</b>	R_G 4				
<b>Req. Name</b>	Factors of safety (FOS)				
<b>Description</b>	All margins of safety shall be applied as specified in [AD-03] and [AD-04].				
<b>References</b>	[AD-02] Chpt. 4.7.5.3	Moc	2	Compliance	C*

<b>Req. ID</b>	R_G 5				
<b>Req. Name</b>	Margin of safety (MOS)				
<b>Description</b>	All margins of safety shall be applied as specified in [AD-03] and [AD-04]. All MOS shall be positive.				
<b>References</b>	[AD-03], [AD-04]	Moc	2	Compliance	C*

<b>Req. ID</b>	R_G 6				
<b>Req. Name</b>	Margin of safety				
<b>Description</b>	MOS=(design allowable load)/(design limit load x FOS)-1				
<b>References</b>	[AD-03], [AD-04]	Moc	2	Compliance	C

## 2.5 Mechanical Requirements

<b>Req. ID</b>	R_M 1				
<b>Req. Name</b>	General Design (1/2)				
<b>Description</b>	All mechanisms shall be designed in compliance to [AD-02].				
<b>References</b>	User	Moc	0	Compliance	C*

<b>Req. ID</b>	R_M 2				
<b>Req. Name</b>	General design (2/2)				
<b>Description</b>	All mechanism shall be designed to function on ground and in thermal vacuum conditions.				
<b>References</b>	[AD-02] Chpt. 4.7.2	Moc	1	Compliance	C*

<b>Req. ID</b>	R_M 3				
<b>Req. Name</b>	Interfaces (1/2)				
<b>Description</b>	The interface shall match to the rover system.				
<b>References</b>	User	Moc	1	Compliance	C

<b>Req. ID</b>	R_M 4				
<b>Req. Name</b>	Interfaces (2/2)				
<b>Description</b>	The arm shall fit inside the allocated area.				
<b>References</b>	User	Moc	1	Compliance	

<b>Req. ID</b>	R_M 5				
<b>Req. Name</b>	Parts and Components				
<b>Description</b>	Existing stepper motors shall be used.				
<b>References</b>	User	Moc	0	Compliance	C

<b>Req. ID</b>	R_M 6				
<b>Req. Name</b>	Mechanism function				
<b>Description</b>	<p>Mechanical interface, position accuracy or velocity tolerances shall be specified and verified that they conform to the functional needs.</p> <p>The envelope of movement for each moving part shall be defined.</p> <p>The movement of each part shall ensure that there is no mechanical interference with any other part of the mechanism, the spacecraft, the payload or the launcher.</p>				
<b>References</b>	[AD-02] Chpt. 4.4.2	Moc	0, 4, 8	Compliance	C

<b>Req. ID</b>	R_M 7				
<b>Req. Name</b>	Operating Temperatures				
<b>Description</b>	The arm shall be operational in a total temperature range of 3D printable polyactide acid (PLA) Filament (-40 °C to 60 °C)				
<b>References</b>	User	Moc	0	Compliance	C

<b>Req. ID</b>	R_M 8				
<b>Req. Name</b>	Functional dimensioning				
<b>Description</b>	Actuators shall be sized to provide throughout the operational lifetime and over the full range of travel actuation torques or forces.				
<b>References</b>	[AD-02] Chpt. 4.7.5.3	Moc	2	Compliance	C

### 3 Robotic arms on Rovers and in space

Even though there are rovers without a robotic arm, the majority of the current rovers are equipped with such manipulator system, due to the flexibility and dexterity of the mechanical system. One of the first prototypes with a robotic arm designed for mars exploration was the *Rocky 7* prototype in 1997 [2]. Over the time the complexity of the robotic arm systems was increased and the arms became more dexterous and universal.

#### 3.1 Robotic Arms

This chapter introduces four robotic arms to represent the current state of robotic arms in the space industry.

The *MER Instrument Positioning System* (Figure 1a) is a dexterous robotic arm with visual target selection and autonomous software functions to position and orient the in-situ instruments. This system was used for the Mars Exploration Rovers Spirit and Opportunity which landed on the Mars in 2004. With a mass of 4 kg and a Range of 0,75 m it is the smallest arm being introduced here. The 5 L-Shape type joints are actuated with a brushed DC motor and planetary gear as transmission [3].

The *Phoenix Mars Lander Robotic Arm* (Figure 1b) acquires samples of Martian dry and icy soil on the Phoenix Mars Lander that landed on Mars in 2008. As the Mars lander is stationary and the requirements on the dexterity of the arm are reduced, only 4 L-shape type joints are necessary. Like the *MER IDD* brushed DC motors with a planetary gear are used, but additionally a harmonic drive was integrated to further increase the output torque. In comparison to the *MER IDD* the harmonic drive was necessary, as the primary function of this arm is a digging application [4].

The *Mars Science Laboratory Robotic Arm* (Figure 1c) is designed to position the required instruments to examine and study the martian soil. It is used on the *Curiosity* rover that landed on Mars in 2012 and is still operating. With a mass of 100 kg it is able to lift the payload of 30 kg and is the heaviest arm compared to the others. In contrary to the *MER IDD* and the *MSLRA* it uses a brushless DC motor [5].

The *DEXARM* (Figure 1d) is still being developed to perform tasks that were originally intended for humans. These applications usually are internal or external servicing of orbiting platforms or robotics for planetary exploration. As it is the most current arm it represents the current state of the art. The seven L-shaped joints are actuated with a brushless DC motor with a hollow shaft which allows for internal cable routing. This possibility and the use of a Bus system for communication and power delivery results in a much lower weight of the harness [6].

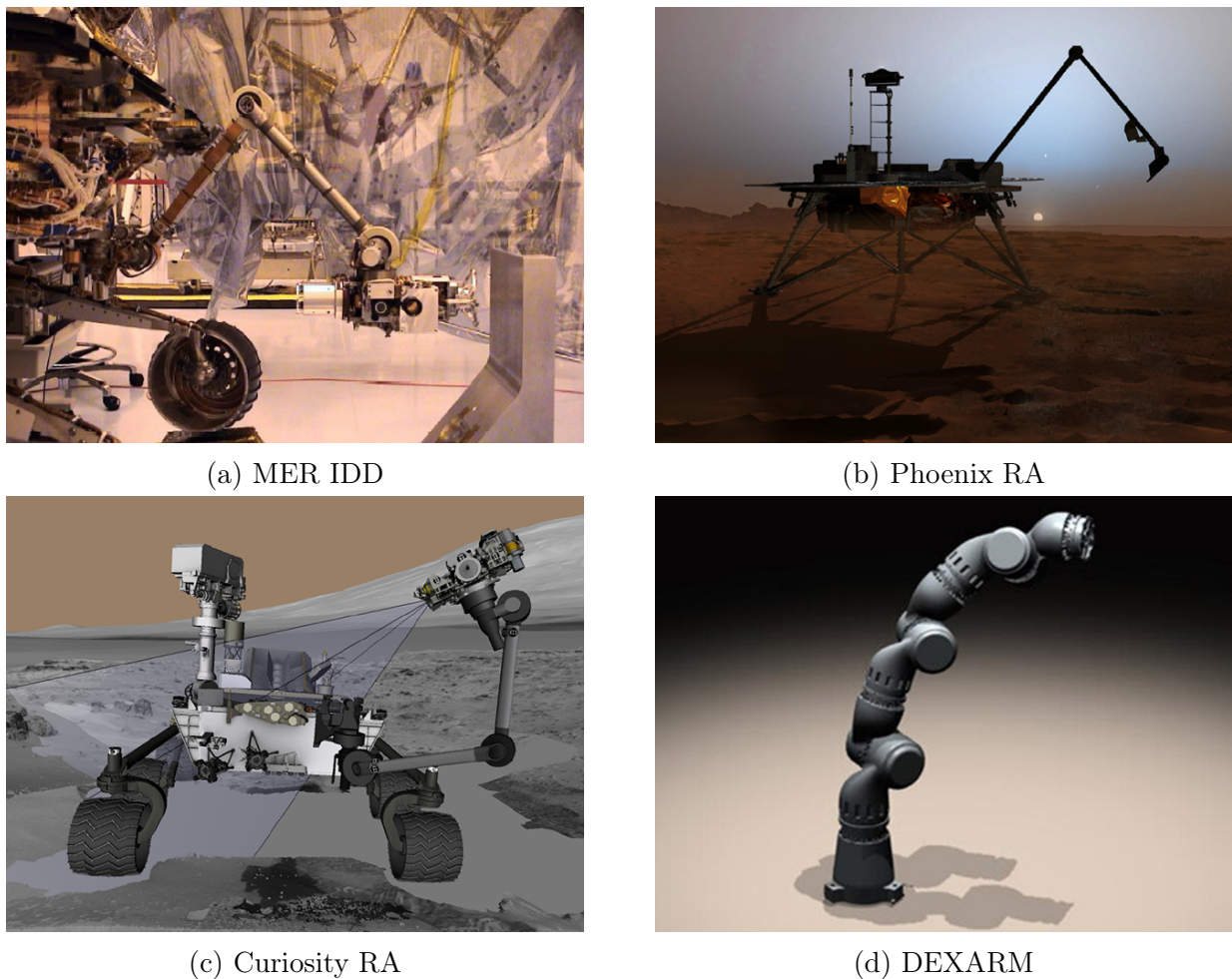


Figure 1: Different Aerospace Robotic Arms

	Mars Exploration Rover Instrument Positioning System	Phoenix Mars Lander Robotic Arm	Mars Science Laboratory Robotic Arm	Dexterous Robot Arm
<b>Abbreviation</b>	MER IDD	Phoenix RA	Curiostiy RA	DEXARM
<b>Range [m]</b>	0,75	2,14	2	1
<b>Mass [kg]</b>	4	-	100	27
<b>Payload [kg]</b>	2	-	30	10
<b>DOF</b>	5	4	5	7
<b>Joint System</b>	L-Shaped	L-Shaped	L-Shaped	L-Shaped
<b>Cables</b>	external	external	external	internal
<b>Bus</b>	no	no	no	yes, Power and Signal
<b>Actuator</b>	brushed DC	brushed DC	brushless DC	brushless DC
<b>Transmission</b>	planetary gear	planetary gear, harmonic drive	planetary gear	harmonic drive

Table 5: Properties of different Aerospace Mechanical Arms

### 3.2 Joint Connection Types and Cable Routing

The actuation of the joints and the transmission of payload data requires cable routing, which has to be integrated into the joint design. Three different possibilities of the interaction between the joint connection type and the cable routing are shown in Figure 2.

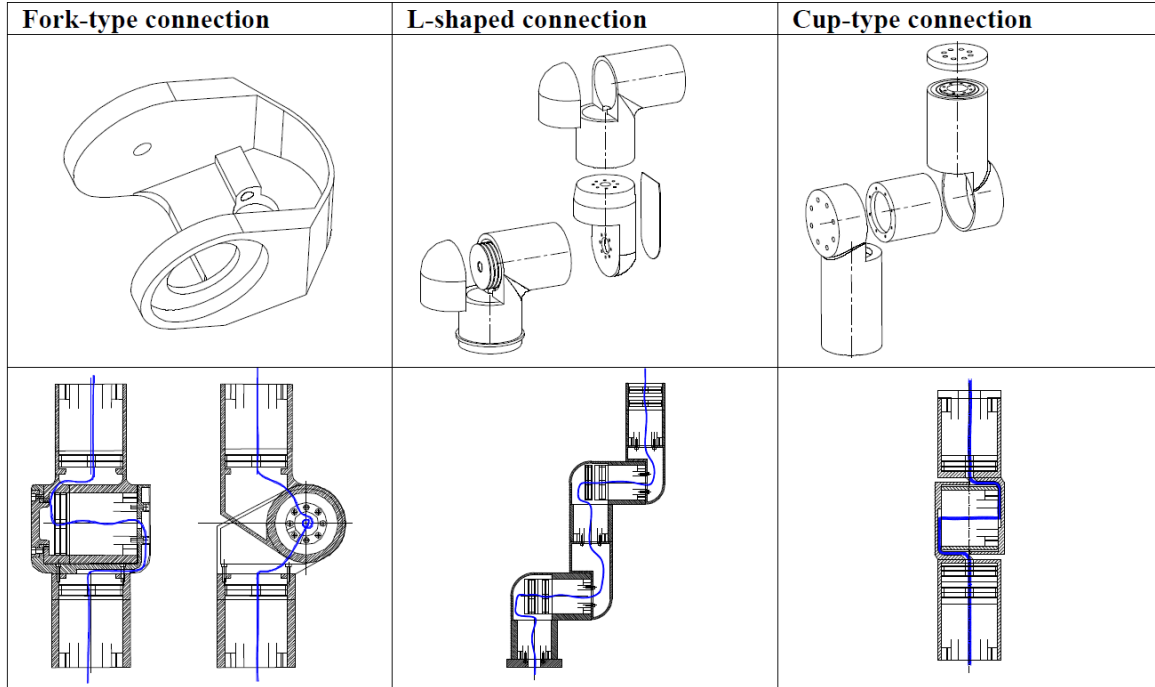


Figure 2: Mechanical solution, cable routing and comparison of the joint connection types [6]

The L-shaped and Cup-type connection can be realized with a simpler shape of mechanical components, whereas the Fork-type connection requires a more complex shape of these parts. Internal cable routing is easiest in the L-shaped connection but all internal cable routing options imply a motor with a hollow shaft. The angular range of a joint is only limited with a Cup-type connection to about  $\pm 90^\circ$  [6].

Due to the angular range limitation of the Cup-type connection and the mechanical part complexity of the Fork-type connection it is clear that the L-shape is the favored configuration (ref. Table 5).

## 4 Pre-Design

### 4.1 Possible Designs

The main task for the arm, as listed in the requirements (ref. Chapter 2), is to grab and place sintered Regolith pavers, which can be realized with multiple designs. In order to choose the best suited design, the different approaches need to be analyzed in regard to their minimal length. The minimal length is defined by the length needed to reach the point where the pavers are stored (*loading point*) and the points where the pavers need to be placed. The length was chosen as an integral value, as it is directly proportional to the weight, which is the decisive value in any space system due its proportionality to launch costs. Following four designs were analyzed:

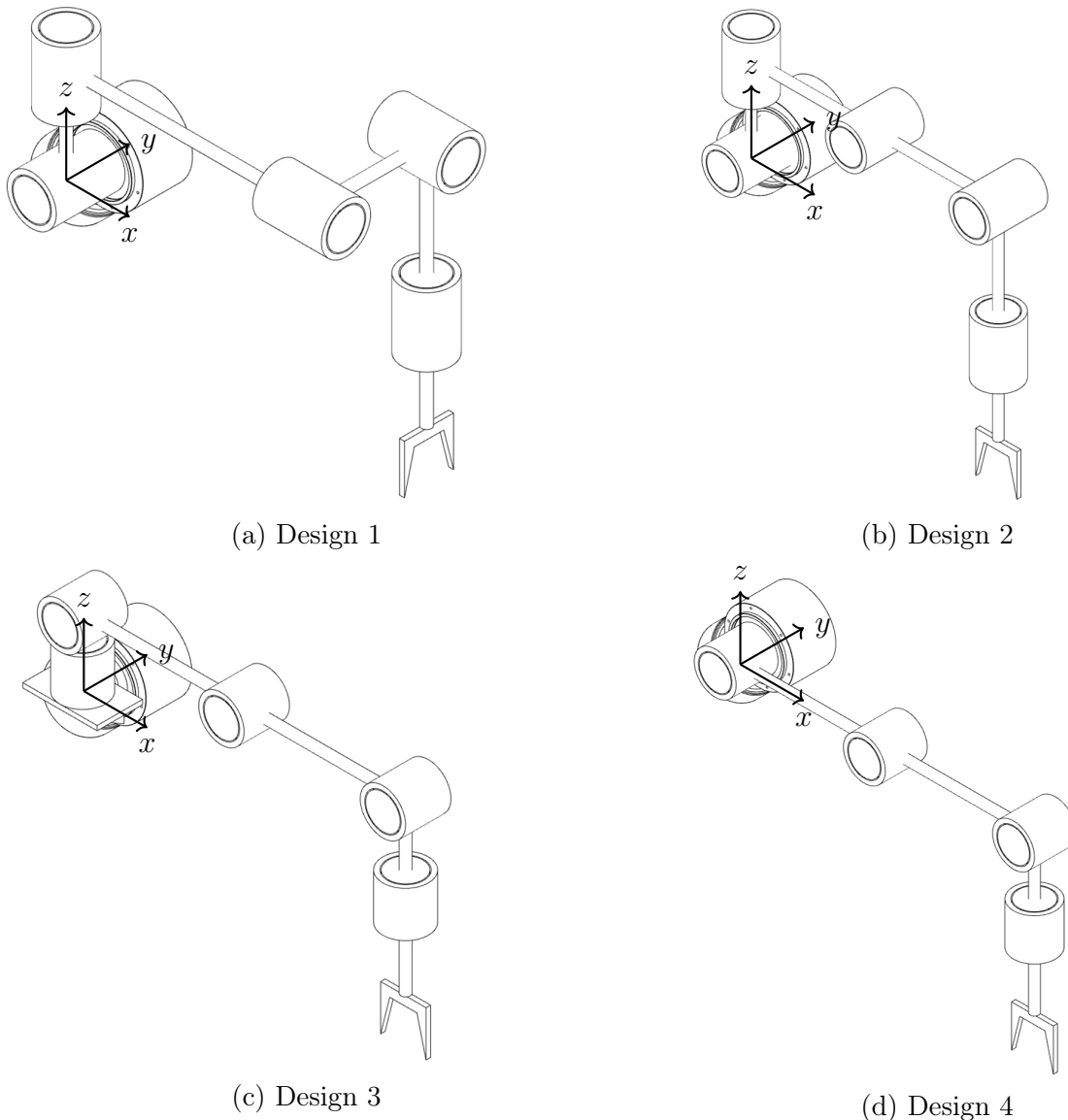


Figure 3: Different Designs for the manipulation system

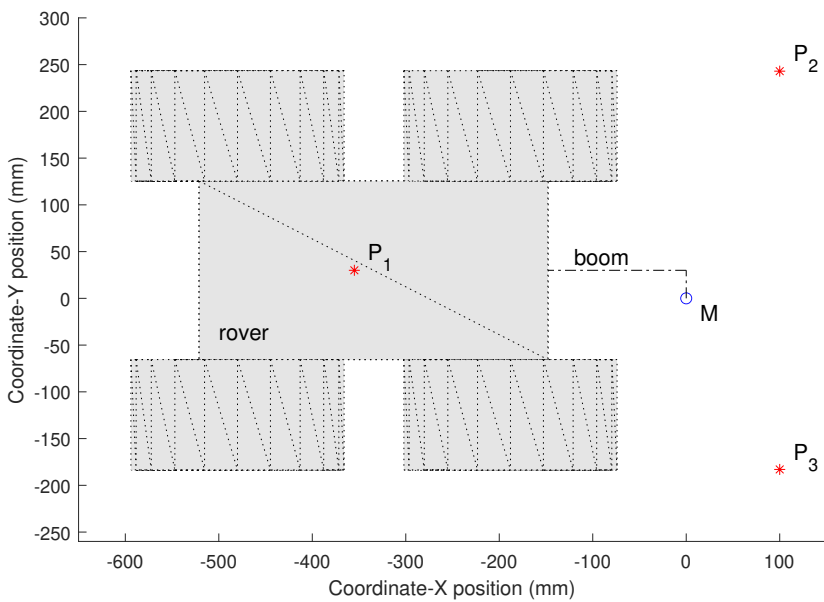
The main difference between those designs is the revolution axis of the first joint. The first joint of design 1,2 and 4 revolve around the y-axis whereas the first joint of design 3 revolves around the z-axis. When choosing the y-axis as first axis of rotation, the end effector can not be placed orthogonal to the surface, except when the arm only rotates around the z-axis (no rotation around the y-axis).

Design 4 therefore eliminates the joint and becomes a 4 degrees of freedom (DOF) arm. With only 4 joints, the arm can now only operate in one plane and is no longer able to position the end effector in 3 dimensions.

Design 3 requires an additional mount at the side of the rover boom. The first joint revolves around the z-axis granting the arm the ability to place the end-effector in 3-dimensions while still being able to place the end effector orthogonal to the ground surface.

## 4.2 Pre-Design Calculations

The following chapter calculates the minimal required length (integral value) of any design while still satisfy the requirements. To calculate this variable, an additional requirement was formulated: each design needs to be able to reach three specific points.



- $P_1$ : Loading point (point where the pavers are placed on top of the rover)
- $P_2$ : Left most point on the ground
- $P_3$ : right most point on the ground
- $M$ : mounting point for arm

Figure 4: required points for the design to reach

### 4.2.1 Forward Kinematics

There are different approaches for a robotic arm to calculate the position of the end effector and to calculate the required angles with a given position and orientation of the end effector. The calculation of the position of the end effector with given angles for each joint is called Forward Kinematics. The end position can be calculated via a geometric approach and via the *Denavit-Hartenberg* (DH) method [7]. The geometric approach is generally the fastest method but can become increasingly complex with increasing DOF. Even though design 1-3 include the

same 5 DOF manipulation system, the geometric approach is only suitable for design 3. For design 1 and 2 the *Denavit-Hartenberg* method has to be used for the Forward Kinematics.

#### 4.2.2 Denavit-Hartenberg Method

The DH parameters describe the location and orientation of each link frame in correlation to each other. The following table lists these parameters exemplary for design 1.

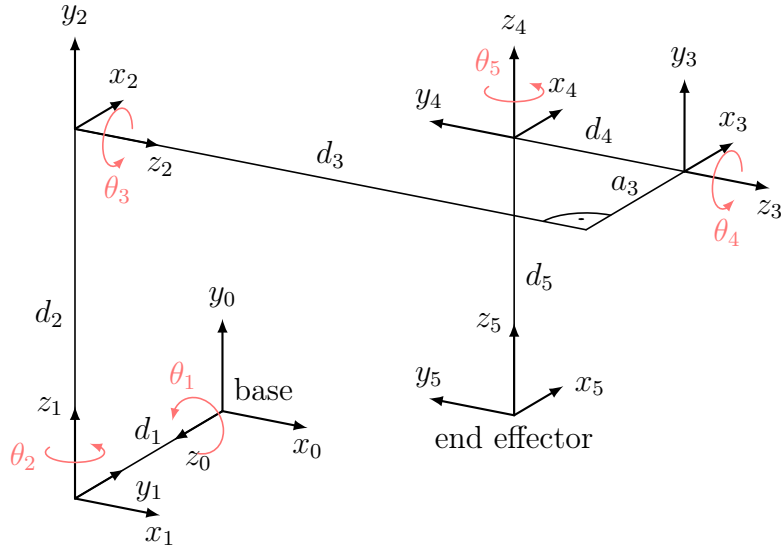


Figure 5: Coordinate Frames Design 1 for DH Parameters

Frame No.	$\theta$	$\alpha$	a	d
1	$\theta_1$	-90°	0	$d_1$
2	$\theta_2 + 90^\circ$	90°	0	$d_2$
3	$\theta_3$	0	$a_3$	$d_3$
4	$\theta_4$	-90°	0	$-d_4$
5	$\theta_5$	0	0	$-d_5$

Table 6: DH parameters for Design 1

With these parameters the transformation matrix  $T_i$  between two neighboring frames  $B_{i-1}$  and  $B_i$  is expressed with the following equation [7]:

$${}^{i-1}T_i = \begin{bmatrix} \cos \theta_i & -\sin \theta_i \cos \alpha_i & \sin \theta_i \sin \alpha_i & a_i \cos \theta_i \\ \sin \theta_i & \cos \theta_i \cos \alpha_i & -\cos \theta_i \sin \alpha_i & a_i \sin \theta_i \\ 0 & \sin \alpha_i & \cos \alpha_i & d_i \\ 0 & 0 & 0 & 1 \end{bmatrix} \quad (1)$$

The forward kinematics is the result of the combined transformation matrix.

$${}^0T_n = {}^0T_1(q_1) {}^1T_2(q_2) {}^2T_3(q_3) \dots {}^{n-1}T_n(q_n) \quad (2)$$

By substituting the parameters from Table 6 in (2) the general transformation matrix from the first joint to the end effector is derived.

$${}^0T_5 = \begin{bmatrix} l_x & m_x & n_x & p_x \\ l_y & m_y & n_y & p_y \\ l_z & m_z & n_z & p_z \\ 0 & 0 & 0 & 1 \end{bmatrix} \quad (3)$$

$$l_x = -c_5(s_4(c_3s_1 + c_1c_2s_3) + c_4(s_1s_3 - c_1c_2c_3)) - c_1s_2s_5 \quad (4)$$

$$l_y = c_5(s_4(c_1c_3 - c_2s_1s_3) + c_4(c_1s_3 + c_2c_3s_1)) - s_1s_2s_5 \quad (5)$$

$$l_z = -c_2s_5 - c_5(c_3c_4s_2 - s_2s_3s_4) \quad (6)$$

$$m_x = s_5(s_4(c_3s_1 + c_1c_2s_3) + c_4(s_1s_3 - c_1c_2c_3)) - c_1c_5s_2 \quad (7)$$

$$m_y = -s_5(s_4(c_1c_3 - c_2s_1s_3) + c_4(c_1s_3 + c_2c_3s_1)) - c_5s_1s_2 \quad (8)$$

$$m_z = s_5(c_3c_4s_2 - s_2s_3s_4) - c_2c_5 \quad (9)$$

$$n_x = s_4(s_1s_3 - c_1c_2c_3) - c_4(c_3s_1 + c_1c_2s_3) \quad (10)$$

$$n_y = c_4(c_1c_3 - c_2s_1s_3) - s_4(c_1s_3 + c_2c_3s_1) \quad (11)$$

$$n_z = c_3s_2s_4 + c_4s_2s_3 \quad (12)$$

$$\begin{aligned} p_x = & d_5(s_4(s_1s_3 - c_1c_2c_3) - c_4(c_3s_1 + c_1c_2s_3)) - d_2s_1 + c_1d_3s_2 + c_1d_4s_2 - a_3s_1s_3 \\ & + c_1c_2c_3a_3 \end{aligned} \quad (13)$$

$$\begin{aligned} p_y = & c_1d_2 - d_5(s_4(c_1s_3 + c_2c_3s_1) - c_4(c_1c_3 - c_2s_1s_3)) + c_1a_3s_3 + d_3s_1s_2 + d_4s_1s_2 \\ & + c_2c_3a_3s_1 \end{aligned} \quad (14)$$

$$p_z = d_1 + c_2d_3 + c_2d_4 + d_5(c_3s_2s_4 + c_4s_2s_3) - c_3a_3s_2 \quad (15)$$

with  $c_i = \cos \theta_i, s_i = \sin \theta_i$

The matrix  $\{(l_x, l_y, l_z), (m_x, m_y, m_z), (n_x, n_y, n_z)\}$  describes the orientation and the vector  $(p_x, p_y, p_z)$  the location of the end effector. The combination of the equations (3) - (15) is the solution for the Forward Kinematics calculated via the DH method.

#### 4.2.3 Geometric Approach

As mentioned the Forward Kinematics can also be determined with a geometric approach which is presented in the following chapter on design 3. As seen in Figure 6 the arm can be seen as a 3R planar manipulator robot with an additional joint around the z-Axis at the base (joint 1) and another joint for rotating the end effector (joint 5). The sole purpose of joint 5 is the alignment of the orientation of the pavers on the x-y plane and is therefore not contributing to the positioning of the end effector. Joint 1 makes the 3R planar manipulator a 4R 3D manipulator.

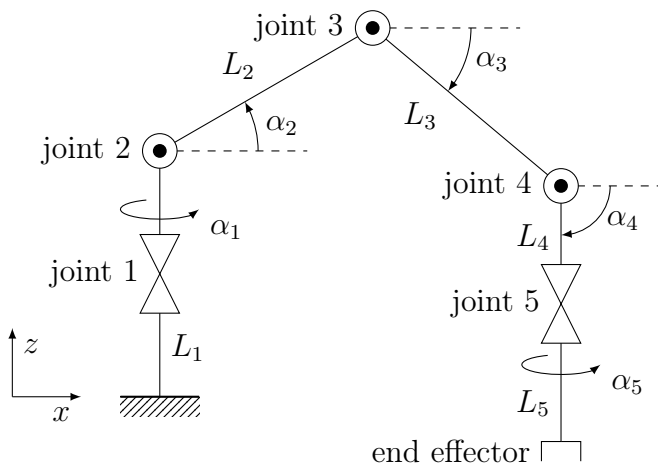


Figure 6: Kinematic Structure of Design 3

To simplify the kinematic system even more, it is requested for the last link of the arm to be perpendicular to the ground surface ( $\alpha_4 \stackrel{!}{=} 90^\circ$ ). Therefore the joint 4 isn't contributing to the positioning of the end effector as well. The solution of the forward kinematics of this design is therefore only the placement of joint 4 above the required end position.

The equations to describe the systems are:

$$\text{joint } 2, P_1 : x_1 = 0 \quad (16)$$

$$y_1 = 0 \quad (17)$$

$$z_1 = L_1 \quad (18)$$

$$\text{joint } 3, P_2 : x_2 = x_1 + \cos \alpha_1 L_2 \quad (19)$$

$$y_2 = y_1 + \sin \alpha_1 L_2 \quad (20)$$

$$z_2 = z_1 + \cos \alpha_2 L_2 \quad (21)$$

$$\text{joint } 4, P_3 : x_3 = x_2 + \cos \alpha_1 L_3 \quad (22)$$

$$y_3 = y_2 + \sin \alpha_1 L_3 \quad (23)$$

$$z_3 = z_2 + \cos \alpha_3 L_3 \quad (24)$$

With any given End Point  $P_e$  the equation system can be solved. The result of which is the solution for the Forward Kinematics of Design 3.

$$x_3 \stackrel{!}{=} P_{e,x} \quad (25)$$

$$y_3 \stackrel{!}{=} P_{e,y} \quad (26)$$

$$z_3 \stackrel{!}{=} P_{e,z} + L_4 + L_5 \quad (27)$$

#### 4.2.4 Inverse Kinematics

The forward kinematics describe the position of the end effector for given joint angles. To calculate the minimal required length for the manipulator, the inverse kinematics has to be determined. With the inverse kinematics the joint angles are calculated for a given point. The problem of solving the inverse kinematics can also be solved in multiple ways. Closed form solutions e.g algebraic and geometric or numerical methods such as the *Jacobian Transpose method*, *Pseudoinverse method* and *Damped Least Squares method* [8]. Although it is possible

to solve the DH forward kinematics solution algebraically [9], this thesis chose another quasi-numerical approach for design 1. For design 3 and 4 the geometric method is used.

#### 4.2.5 Geometric Method

The geometric method is exemplary shown in the following chapter on design 3. The existing task is an optimization problem with boundary conditions. The Optimization is the minimizing of the length while satisfying the constraints. The constraints are the reaching of the required points  $P_1 - P_3$  (ref. Figure 4) and the present joint limits. To solve such problem the nonlinear optimization function *fmincon* of the program *MATLAB* is used.

```
1 [x, fval] = fmincon(@goalFun, x0, A, B, Aeq, Beq, LB, UB, @nonlcon);
```

Figure 7: non linear optimization solver in *MATLAB*

This function tries to minimize the value of the specified function *goalFun* while varying the variable  $x$  within the given boundaries  $LB, UB$  while satisfying the linear  $A, B, Aeq, Beq$  and non-linear *nonlcon* inequality and equality constraints. As the defined problem is non-linear, the equations (16) - (27) are defined in the *nonlcon* function.

The solver was not able to find a solution for all three points at the same time, so the problem was split in finding a solution for the points in front ( $P_2, P_3$ ) and the point on the back of the rover ( $P_1$ ). The defining minimal length is the bigger of those two. To verify that the corresponding other point can be reached, the solver must be called again with the limiting minimal length. For design 3  $P_1$  is the constraining point which results in a minimal length of  $L_{min} = 657,3$  mm with the following link lengths.

Link	$L_1$	$L_2$	$L_3$	$L_4$	$L_5$
Length in [mm]	85	85	271,3	108	108

Table 7: Links length for Design 3 with minimal total length

A visual representation of the solution is given in Figure 8 and the complete *MATLAB* script can be found in the digital appendix.

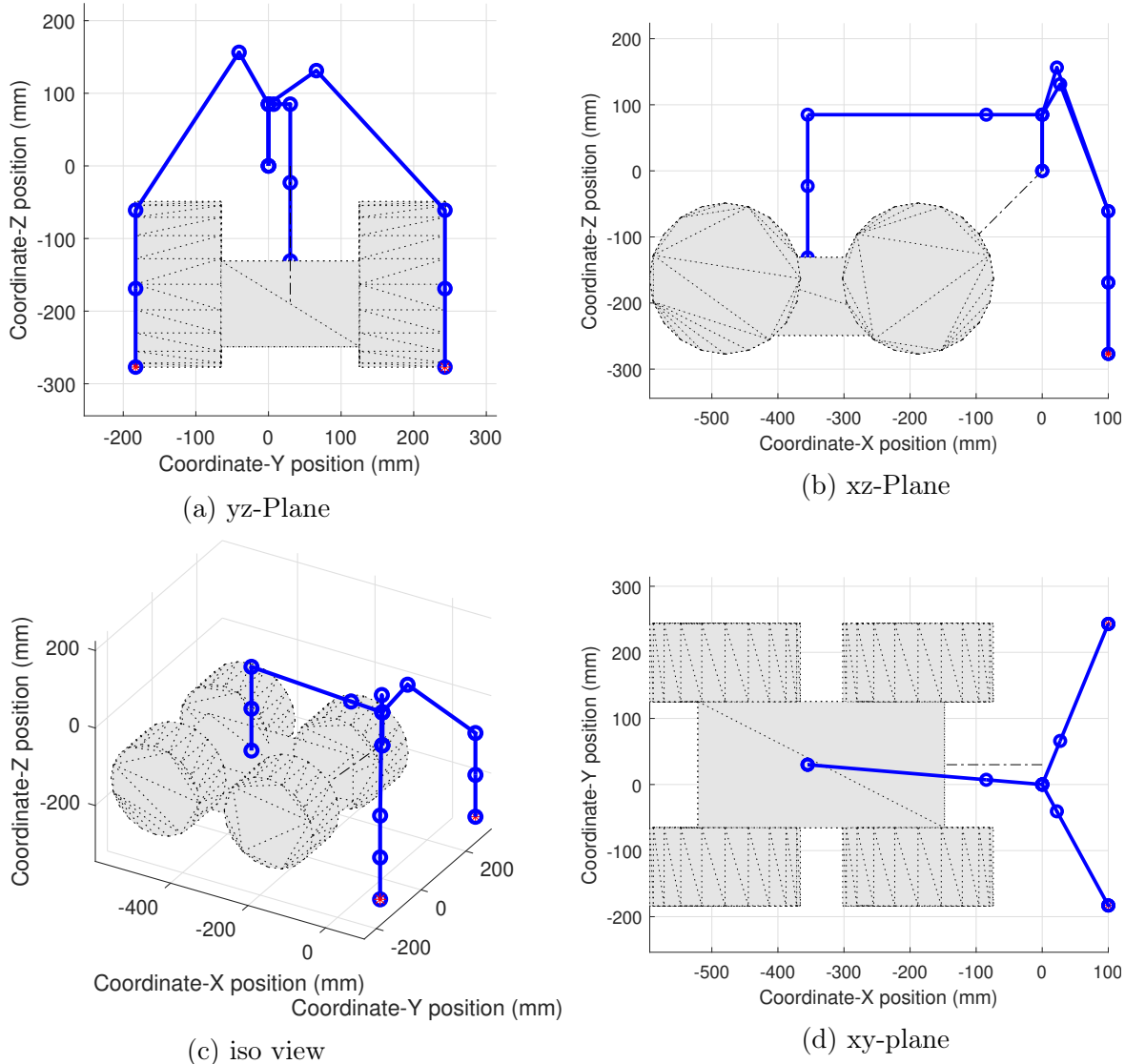


Figure 8: Result of the Length Optimization Design 3

The calculation for design 4 is analogous to design 3, but because of the kinematics only in two dimensions. Similar to design 3, the loading point  $P_1$  was the driving length and results in a total length of  $L_{min} = 475,2$  mm. The corresponding link lengths and arm state are displayed below.

Link	$L_1$	$L_2$	$L_3$	$L_4$
Length in [mm]	177,6	177,6	60	60

Table 8: Links length for Design 4 with minimal total length

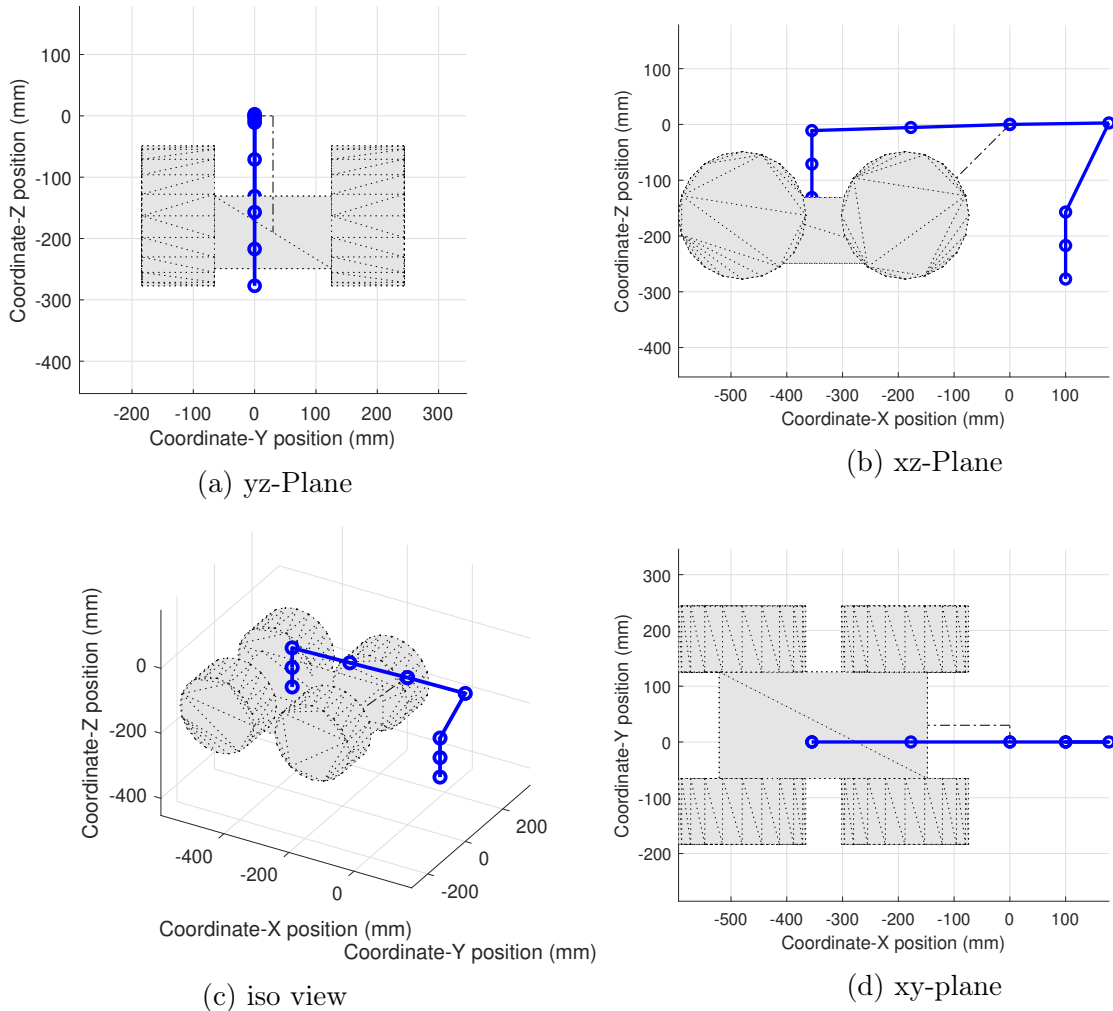


Figure 9: Result of the Length Optimization Design 4

#### 4.2.6 Quasi Numerical Method

To keep the complexity for this preliminary design study low, the inverse kinematics for design 3 and 4 have not been determined. If one of these designs are chosen for further development, the final inverse kinematics needs to be calculated in order to control the system. But in this study a quasi numerical method in *MATLAB* was developed. The general idea behind this approach is to calculate the workspace of the manipulator by varying the angles and calculate the final result in a point cloud (Figure 10). When a specific point needs to be reached, the nearest point in the calculated point cloud is chosen and the corresponding angles used. This method results in an error depending on the density of the point cloud and is to be considered.

The first step in *MATLAB* is to create a set of DH parameters (ref. subsubsection 4.2.2). The angles  $\theta_1 - \theta_5$  are set to cover a specific range. During the calculation of the workspace each possible combination of angles is calculated and the resulting end effector position stored in a final matrix. The end effector position is hereby calculated with the equations (13)-(15) as the orientation arises as a result of the previous points and a visual representation is sufficient for this study.

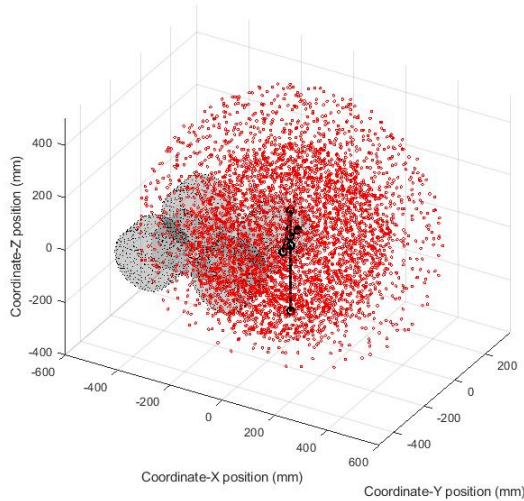


Figure 10: workspace as point cloud

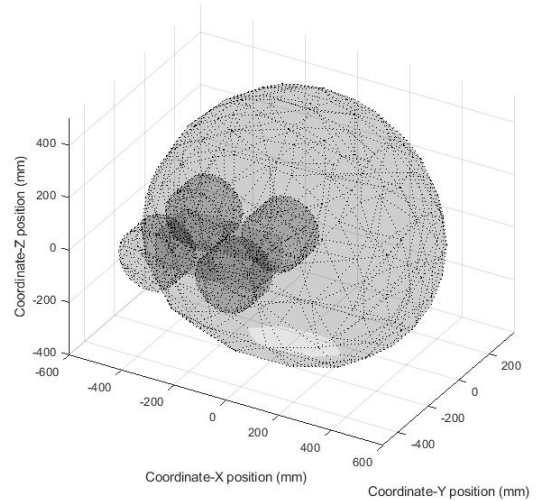


Figure 11: hull around workspace

To find the shortest length of the arm for this design, the length has to be varied as well. To implement this behavior and create an optimization program the above described procedure is extended. If the lengths were also ranged similar to the angles, the resulting matrix would be too large to manually evaluate. Therefore the algorithm needs to be adjusted. When trying all possible combinations of lengths in a certain range, there are many possible combination in which the resulting arm is not able to reach the desired point. Additionally as only specific points are calculated the arm would just reach the exact point by coincidence. So the algorithm needs to differentiate between these two cases (physically not reachable, physically reachable but missed by chance). The program lays a hull around the workspace and subsequently calculates the intersection between this hull and the ground surface (Figure 11).

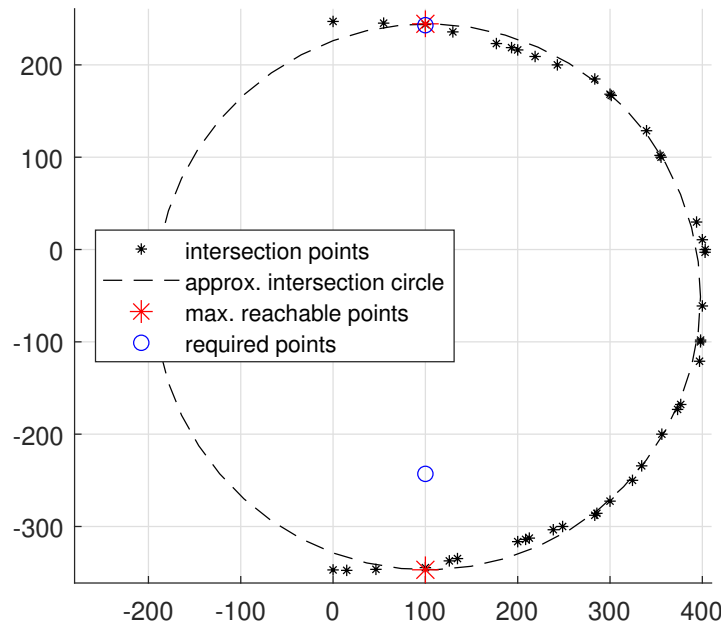


Figure 12: intersection check

A circle is approximated to this intersection line and it is checked whether the required points are inside approximated circle. This condition is saved in the final matrix as well as the total length of the arm, the lengths of the individual links and the corresponding angles. After the algorithm went through all possible combination of lengths and angles in the given range, the combination with the shortest total length is displayed. For design 1 this resulted in a total length of  $L = 717$  mm and an average point error of  $e = 70,7$  mm. This error is the accuracy of the algorithm and could be reduced by further increasing the point density in the point cloud. Due to the high calculation time needed for this, this is not done for this study.

Link	$L_1$	$L_2$	$L_3$	$L_4$	$L_5$
Length in [mm]	100	250	117	100	150

Table 9: Links length for Design 1 with minimal total length

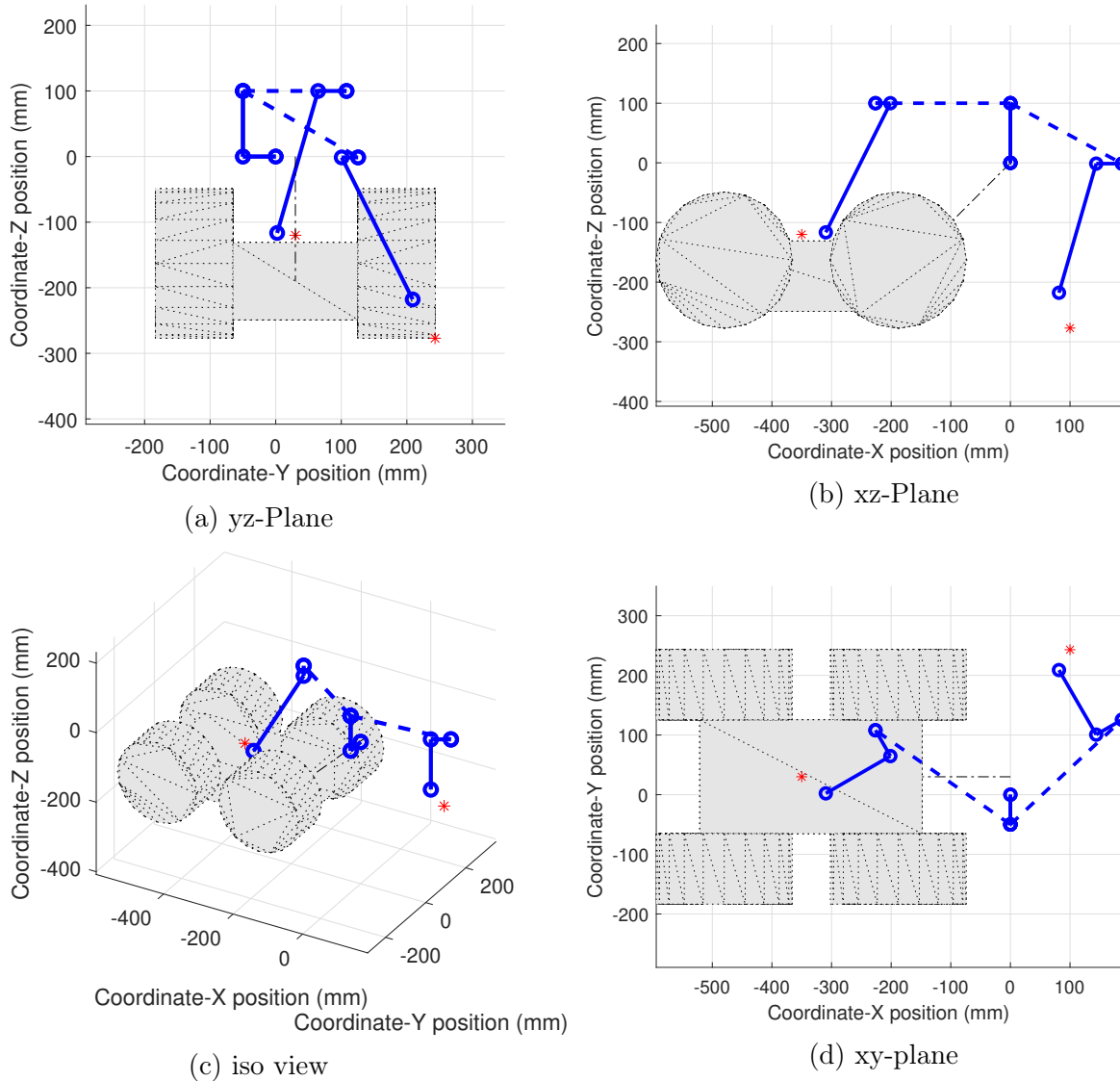


Figure 13: Result of the Length Optimization Design 1

## 4.3 Design Selection

### Design 1&2

These designs have a very complex kinematics which can be solved via DH parameters and a pseudo numerical approach. Nonetheless, due to the joint sequence they are not able to place the end effector perpendicular to the ground surface. Only when the arm is completely in the xz-Plane, the arm is perpendicular to the ground surface, which makes one joint unnecessary. In this case the rover would have to position itself sideways very accurately. Due to the ability to operate in 3D space a collision with the counterbalance weight is possible, which needs to be checked in the controls of the arm. Design 1 and 2 respectively would require the longest arm in order to reach the required points (see. Table 10).

### Design 3

This is the most dexterous design. It is able to place the end effector perpendicular to the ground surface as well as covering the whole front of the rover. Just like design 1&2 a collision check has to be implemented but due to the simple kinematics it is easier to calculate and requires less processing power. The design can not be directly mounted to the knights buckle assembly and requires an additional base. The length is less than Design 1&2, but still more than design 4.

### Design 4

Design 4 is the least dexterous design, as it is only able to operate in the xz-plane, which requires a very accurate sideways positioning of the rover. As it can only be operated in one plane, there is no need to implement a collision control with the counter balance. It is the consequence from design 1&2 with one saved motor and the direct attachment to the knights buckle design.

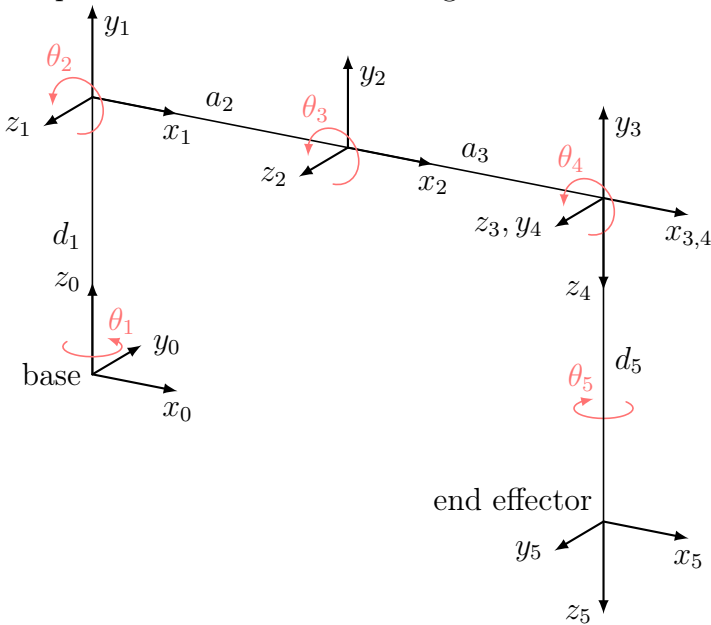
Design No.	Length in [mm]
1	817,0
3	657,3
4	475,2

Table 10: Design Comparison

Design 3 was finally chosen for its dexterity, medium length, and simple kinematic solution.

#### 4.4 First Static and Dynamic Analyses

The next step in a manipulator design is the calculation of the forces and torques, to choose a suitable actuator and to dimension the links. There are two main analyses needed, to calculate these parameters, a static and a dynamic analysis. The static analysis is often used to determine which motors to use, as this is the consistent minimal stress on the joints. After this, the possible accelerations and movement speeds can be determined and it can be decided, whether the chosen motors are still suitable or need to be scaled up. The following analyses are made according to [10]. The described methods are using the DH parameters which need to be determined at first for the chosen design similar to chapter 4.2.2. The frames for the DH parameters are shown in Figure 14 and the corresponding DH parameters in Table 11.



Frame No.	$\theta$	$\alpha$	a	d
1	$\theta_1$	90°	0	$d_1$
2	$\theta_2$	0	$a_2$	0
3	$\theta_3$	0	$a_3$	0
4	$\theta_4$	90°	0	0
5	$\theta_5$	0	0	$d_5$

Table 11: DH parameters for Design 3

Figure 14: Coordinate Frames Design 3 for DH Parameters

For the static analysis the recursive method was used. In this method all the forces and moments acting on the links are determined recursively starting with the loads on the end effector. The acting forces on a typical link are displayed in Figure 15.

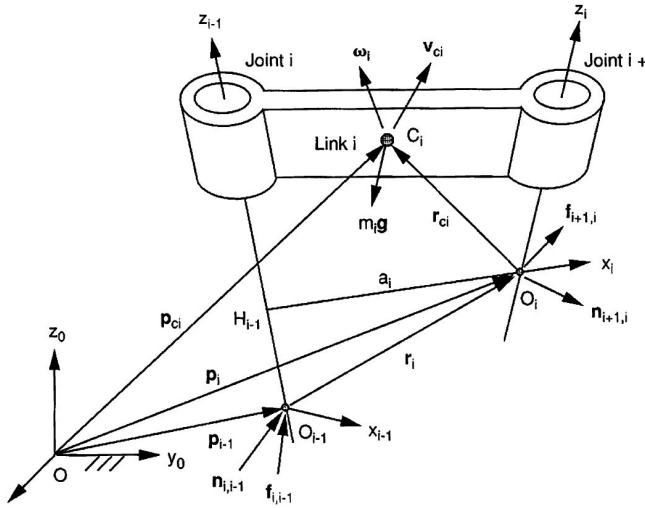


Figure 15: Forces and moments acting on link i [10]

Three forces and two moments are exerted on link  $i$ :  $m_i g$ ,  $f_{i+1,i}$ ,  $f_{i-1,i}$ ,  $n_{i+1,i}$  and  $n_{i-1,i}$ . These can be determined with the following recursive form.

$$f_{i,i-1} = f_{i+1,i} - m_i g \quad (28)$$

$$n_{i,i-1} = n_{i+1,i} + r_i \times f_{i,i-1} - r_{ci} \times m_i g \quad (29)$$

The position vector  $r_{ci}$  and the vector  $r_i$  need to be transformed in the fixed frame:

$$r_{ci} = {}^0 R_i{}^i r_{ci} \quad (30)$$

$$r_i = {}^0 R_i{}^i r_i \quad (31)$$

$$\text{with } {}^i r_i = \begin{bmatrix} a_i \\ d_i s \alpha_i \\ d_i c \alpha_i \end{bmatrix} \quad (32)$$

The resulting equivalent joint torques are

$$\tau_i = z_{i-1}^T n_{i,i-1} \quad (33)$$

$z_{i-1}$  is a unit vector pointing along the positive  $i$ th joint axis. The calculation projects the torques in the joint in the  $z$ -axis. The remaining forces and moments need to be supported by the bearings. The position vectors  ${}^i r_{ci}$  for design 3 are

$${}^1r_{c1} = \begin{bmatrix} 0 \\ -l_1/2 \\ 0 \end{bmatrix}, \quad {}^2r_{c2} = \begin{bmatrix} -l_2/2 \\ 0 \\ 0 \end{bmatrix}, \quad {}^3r_{c3} = \begin{bmatrix} -l_3/2 \\ 0 \\ 0 \end{bmatrix}, \quad {}^4r_{c4} = \begin{bmatrix} 0 \\ 0 \\ l_4/2 \end{bmatrix}, \quad {}^5r_{c5} = \begin{bmatrix} 0 \\ 0 \\ -l_5/2 \end{bmatrix}$$

Equations (28) and (29) calculate the joint reaction forces in the fixed frame. To calculate the forces in the link frames, following equations are used.

$${}^i f_{i,i-1} = {}^i f_{i+1,i} - m_i {}^i g \quad (34)$$

$${}^i n_{i,i-1} = {}^i f_{i+1,i} + {}^i r_i \times {}^i f_{i,i-1} - {}^i r_{ci} \times m_i {}^i g \quad (35)$$

$${}^{i-1} f_{i,i-1} = {}^{i-1} R_i {}^i f_{i,i-1} \quad (36)$$

$${}^{i-1} n_{i,i-1} = {}^{i-1} R_i {}^i n_{i,i-1} \quad (37)$$

$${}^i g = {}^i R_{i-1} {}^{i-1} g \quad (38)$$

With additional external forces, in this case the motor weight at the end of the link, equation (28) and (34) change to

$$f_{i,i-1} = f_{i+1,i} - (m_i + mm_i)g \quad (39)$$

$${}^i f_{i,i-1} = {}^i f_{i+1,i} - (m_i + mm_i) {}^i g \quad (40)$$

where  $mm_i$  is the motor weight of the motor at the end of link i.

The arm needs to be able to operate in earth gravity with a simulated payload weight. The payload is a paver from *NASA Swamp Works* with a mass of  $m_p \approx 5,5$  kg. This paver needs to be handled by the arm in lunar gravity, which results in the payload force at the end effector  $F_p = g_{lun} m_p = 1,625 \cdot 5,5 = 8,94$  N. The rest of the arm sees the earth gravitation with  $g = 9,81$  m/s<sup>2</sup>.

In the *standard configuration* (ref. Figure 14,  $\theta_i = 0$ ) the following torques and forces at the joints are calculated with MATLAB. For the first static analysis the masses of the links and motors are assumed.

Item	Link 1	Link 2	Link 3	Link 4	Link 5	Motor	Payload
Mass [kg]	0,1	0,1	0,2	0,1	0,1	0,24	5,5

Table 12: Assumption of the masses

The following process is an iteration between design and analysis. As the weight and length of the links change during the design process, the stress on the joints changes as well. This first calculation is the starting point of this iteration process. The links have a decreasing weight as the stress on the links is decreased in direction of the end effector. Also it needs to be considered, whether different motors are chosen for the different joints, which would also result in different loads.

Joint	$F_x$	$F_y$	$F_z$	$N_x$	$N_y$	$N_z$
Joint 1	0	0	29,5	0	-7,52	0
Joint 2	0	0	24,2	0	0	7,52
Joint 3	0	0	19,9	0	0	3,38
Joint 4	0	0	15,6	0	0	0
Joint 5	0	0	12,2	0	0	0

Table 13: Static results in the standard configuration. Forces in [N], Torques in [Nm]

As this configuration is not the worst case scenario the same calculations are done in the *stretched configuration*. In this configuration the manipulator is fully stretched to its full extend ( $\theta_4 = 90^\circ$ ) and therefore exerts the maximum torque on joint 2 and the base attachment.

Joint	$F_x$	$F_y$	$F_z$	$N_x$	$N_y$	$N_z$
Joint 1	0	0	29,5	0	-10,17	0
Joint 2	0	0	24,2	0	0	10,17
Joint 3	0	0	19,9	0	0	6,03
Joint 4	0	0	15,6	0	0	2,65
Joint 5	0	0	12,3	0	2,60	0

Table 14: Static results in the stretched configuration. Forces in [N], Torques in [Nm]

For the dynamical analysis the *recursive Newton-Euler formulation* is applied. This formulation includes all the forces acting on the individual links and the resulting dynamical equations therefore include all the forces of constraint between two adjacent links. It consists of a *forward computation* of the velocities and accelerations of each link and a *backward computation* of the forces and moments in each joint [10, p. 386].

## Forward Computation

The following equations are used for the forward computation.

$${}^i\omega_i = {}^iR_{i-1}({}^{i-1}\omega_{i-1} + {}^{i-1}z_{i-1}\dot{\theta}_i) \quad (41)$$

$$\text{where } {}^iR_{i-1} = \begin{bmatrix} c\theta_i & s\theta_i & 0 \\ -c\alpha_i s\theta_i & c\alpha_i c\theta_i & s\alpha_i \\ s\alpha_i s\theta_i & -s\alpha_i c\theta_i & c\alpha_i \end{bmatrix} \quad (42)$$

$${}^i\ddot{\omega}_i = {}^iR_{i-1}({}^{i-1}\ddot{\omega}_{i-1} + {}^{i-1}z_{i-1}\ddot{\theta}_i + {}^{i-1}\omega_{i-1} \times {}^{i-1}z_{i-1}\dot{\theta}_i) \quad (43)$$

$${}^iv_i = {}^iR_{i-1}{}^{i-1}v_{i-1} + {}^i\omega_i \times {}^ir_i \quad (44)$$

$${}^i\dot{v}_i = {}^iR_{i-1}{}^{i-1}\dot{v}_{i-1} + {}^i\dot{\omega}_i \times {}^ir_i + {}^i\omega_i \times ({}^i\omega_i \times {}^ir_i) \quad (45)$$

$${}^i\dot{v}_{ci} = {}^i\dot{v}_i + {}^i\omega_i \times {}^ir_{ci} + {}^i\omega_i \times ({}^i\omega_i \times {}^ir_{ci}) \quad (46)$$

$${}^ig = {}^iR_{i-1}{}^{i-1}g \quad (47)$$

The above equations describe the *Angular Velocity Propagation* (41), the *Angular Acceleration Propagation* (43), the *Linear Velocity Propagation* (44), the *Linear Acceleration Propagation* (45), the *Linear Acceleration of the Center of Mass* (46) and the *Acceleration of Gravity* (47).

## Backward Computation

The following equations are used for the backward computation.

$${}^i f_i^* = -m_i {}^i \dot{v}_{ci} \quad (48)$$

$${}^i n_i^* = {}^i I_i {}^i \dot{\omega}_i - {}^i \omega_i \times ({}^i I_i {}^i \omega_i) \quad (49)$$

$${}^i f_{i,i-1} = {}^i f_{i+1,i} - m_i {}^i g - {}^i f_i^* \quad (50)$$

$${}^i n_{i,i-1} = {}^i n_{i+1,i} + ({}^i r_i + {}^i r_{ci}) \times {}^i f_{i,i-1} - {}^i r_{ci} \times {}^i f_{i+1,i} - {}^i n_i^* \quad (51)$$

$${}^{i-1} f_{i,i-1} = {}^{i-1} R_i {}^i f_{i,i-1} \quad (52)$$

$${}^{i-1} n_{i,i-1} = {}^{i-1} R_i {}^i n_{i,i-1} \quad (53)$$

For the end effector link  ${}^n f_{n+1,n}$ ,  ${}^n n_{n+1,n}$  represent the end effector output force and moment therefore the external loads on the end effector. Similar to the static analysis the weight of the motors needs to be implemented in equation (50) and (51) as well.

$${}^i f_{i,i-1} = {}^i f_{i+1,i} - (m_i + mm_i) {}^i g - {}^i f_i^* \quad (54)$$

$${}^i n_{i,i-1} = {}^i n_{i+1,i} + ({}^i r_i + {}^i r_{ci}) \times {}^i f_{i,i-1} - {}^i r_{ci} \times ({}^i f_{i+1,i} - mm_i {}^i g) - {}^i n_i^* \quad (55)$$

## Joint Torque Equations

The actuator forces  $\tau_i$  are obtained while projecting the forces onto their corresponding joint axis.

$$\tau_i = {}^{i-1} n_{i,i-1}^T {}^{i-1} z_{i-1} + b_i \dot{\theta}_i \quad (56)$$

where  $b_i$  is the damping coefficient for joint  $i$  when there are viscous forces in the joints.

It is assumed, that the links are cylindrical tubes and therefore the moments of inertia are:

$${}^i I_i = \begin{bmatrix} \frac{1}{12}m(3(r_2^2 + r_1^2) + h^2) & 0 & 0 \\ 0 & \frac{1}{12}m(3(r_2^2 + r_1^2) + h^2) & 0 \\ 0 & 0 & \frac{1}{2}m(r_2^2 + r_1^2) \end{bmatrix} \quad (57)$$

where  $r_1$  is the inner radius,  $r_2$  the outer radius and  $h$  the length of the cylinder. The z-axis is the rotation axis of the cylinder. These moments of inertia are only a rough estimation and need to be replaced later by the actual moments of inertia from the CAD.

When applying no acceleration and rotation on the system, the *recursive Newton-Euler* formulation needs to generate the same results as the static analysis. Referring to Table 15 the results

are indeed identical but it has to be noted, that the static analysis refers to the individual link frame and the dynamical analysis in this case to the base frame.

Joint	$F_x$	$F_y$	$F_z$	$N_x$	$N_y$	$N_z$
Joint 1	0	29,5	0	0	-10,17	0
Joint 2	0	24,2	0	0	0	10,17
Joint 3	0	19,9	0	0	0	6,03
Joint 4	15,6	0	0	0	0	2,65
Joint 5	12,3	0	0	0	2,60	0

Table 15: Dynamical results in the stretched configuration while stationary

For the cross section analysis the worst case loads need to be known. The static analysis provides one bending moment on each individual link. As soon as there are dynamic effects, additional moments appear. For the first rough section analysis these additional moments need to be determined. If a deceleration of  $\ddot{\theta}_1 = \pi/(10 \cdot 2)$  is applied, the following moments act on each joint and link in the *stretched configuration*. This deceleration corresponds to a rotation speed of  $\dot{\theta}_1 = \pi/10$  which is decelerated in 2 seconds. The arm would take 10 seconds for half a rotation.

Joint	$F_x$	$F_y$	$F_z$	$N_x$	$N_y$	$N_z$
Joint 1	0	29,5	-25,8	-2,19	-10,17	9,43
Joint 2	0	24,2	-25,8	0	9,43	10,17
Joint 3	0	19,9	-23,0	0	5,05	6,03
Joint 4	15,6	-14,6	0	0	1,68	2,65
Joint 5	12,3	-8,1	0	1,33	2,60	0

Table 16: Dynamical results in the stretched configuration while decelerating

It can be seen that the additional moment is roughly the same magnitude as the moment resulting from the static analysis. When the arm is in the *standard configuration* additional moments are exerted.

Joint	$F_x$	$F_y$	$F_z$	$N_x$	$N_y$	$N_z$
Joint 1	0	29,5	-22,4	-0,69	-7,52	6,57
Joint 2	0	24,2	-22,4	1,21	6,54	7,52
Joint 3	0	19,9	-19,6	1,21	2,79	3,38
Joint 4	0	-11,2	-15,6	1,21	0,0	0
Joint 5	0	-5,6	-12,3	0,91	0	0

Table 17: Dynamical results in the standard configuration while decelerating

The overall torques are smaller but an additional torque  $N_x = 1,21 \text{ Nm}$  is applied to joint 2-4. Due to the DH convention the frames lay different for each link. Therefore the torques around the individual axis may exert a bending or a torsional moment, depending on the link frame. Table 18 displays which Torque corresponds to which stress.

<b>Joint</b>	<b><math>N_x</math></b>	<b><math>N_y</math></b>	<b><math>N_z</math></b>
Joint 1	$M_{b2}$	$M_{b1}$	$M_t$
Joint 2	$M_t$	$M_{b2}$	$M_{b1}$
Joint 3	$M_t$	$M_{b2}$	$M_{b1}$
Joint 4	$M_{b2}$	$M_t$	$M_{b1}$
Joint 5	$M_{b2}$	$M_{b1}$	$M_t$

Table 18: Bending and Torsion moment distribution

where  $M_{b1}$  is the main bending moment due to gravity,  $M_{b2}$  is the additionally bending moment due to dynamical effects and  $M_t$  is the torsional moment due to dynamical effects. Table 17 is rearranged according to Table 18 and the relations  $f_{b2} = M_{b2}/M_{b1}$  and  $f_t = M_t/M_{b1}$  are calculated.

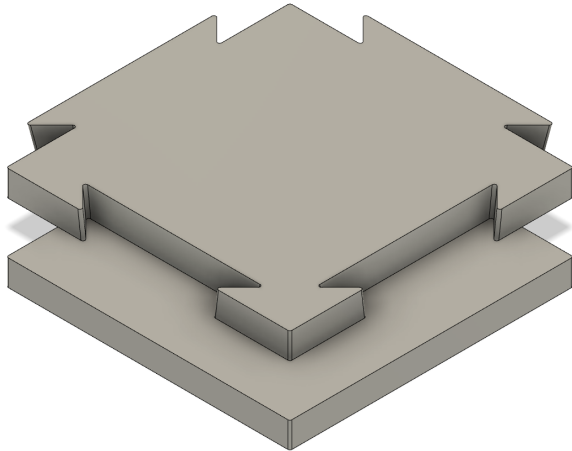
<b>Joint</b>	<b><math>M_{b1}</math></b>	<b><math>M_{b2}</math></b>	<b><math>M_t</math></b>	<b><math>f_{b2}</math></b>	<b><math>f_t</math></b>
Joint 1	-7,52	-0,69	6,48	0,09	-0,86
Joint 2	-7,52	6,48	1,21	0,86	0,16
Joint 3	3,38	2,74	1,21	0,81	0,36
Joint 4	0	1,21	0	-	-
Joint 5	0	0,91	0	-	-

Table 19: Bending and Torsion moments and Factors

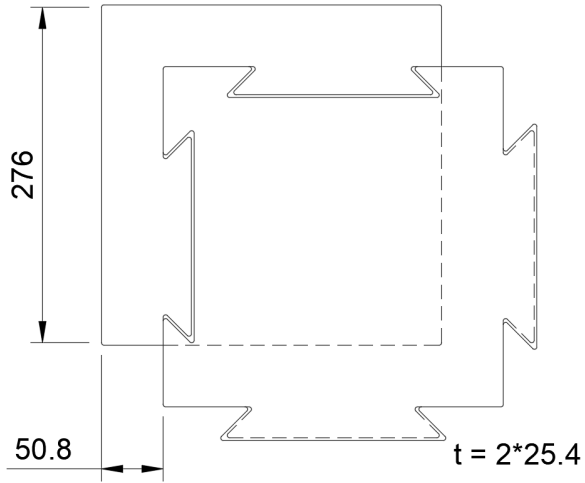
In the standard configuration, joint 4 and 5 are only loaded with the bending moment due to dynamical effects and no factor can be calculated. In the design, the links 1, 4 and 5 are so short, that the link consists only of the motor and transmission mount, therefore no link is required. The two links 2 and 3 are the main concerns for the section analysis.

## 4.5 Second Iteration

The first Analyses were made with the assumption, that the paver has a mass of 1kg. To calculate the approximate mass of the paver it was designed according to pictures. The detailed design is not accessible due to export laws in the USA. The paver is composed of two rectangles with a thickness of 25,4 mm each, one shifted diagonally by 50,8 mm. The interlocking between the pavers is achieved by a vertical motion.



(a) underside of the CAD model



(b) dimensions of CAD model

Figure 16: Dummy paver for arm calculations

The presumed density of the regolith material, which is used to print the paver, is  $\rho = 2 \text{ g/cm}^3$ . With a design factor of safety  $FOS = 1,2$  the final mass of the paver is deduced to be  $m = FOS \cdot 8 \text{ kg} = 9,6 \text{ kg}$ . The design allows the arm to have an inaccuracy of about 10 mm.

To accommodate the larger paver a new length calculation with equal sized Link 2 and 3 has been made.

Link	$L_1$	$L_2$	$L_3$	$L_4$	$L_5$
Length in [mm]	70,1	224,6	224,6	78,4	78,4

Table 20: Link lengths for the second iteration

The loads on the designs changed to

<b>Joint</b>	<b><math>F_x</math></b>	<b><math>F_y</math></b>	<b><math>F_z</math></b>	<b><math>N_x</math></b>	<b><math>N_y</math></b>	<b><math>N_z</math></b>
Joint 1	0	36,2	0	0	-15,44	0
Joint 2	0	30,9	0	0	0	15,44
Joint 3	0	26,59	0	0	0	8,72
Joint 4	22,27	0	0	0	0	2,97
Joint 5	18,94	0	0	0	2,93	0

Table 21: Second Iteration: stretched configuration, stationary

<b>Joint</b>	<b><math>M_{b1}</math></b>	<b><math>M_{b2}</math></b>	<b><math>M_t</math></b>	<b><math>f_{b2}</math></b>	<b><math>f_t</math></b>
Joint 1	-12,47	-0,87	10,3	0,07	-0,83
Joint 2	-12,47	10,3	1,11	0,83	0,09
Joint 3	5,75	4,36	1,11	0,76	0,19
Joint 4	0	1,11	0	-	-
Joint 5	0	0,83	0	-	-

Table 22: Bending and Torsion moments and Factors

## 4.6 Section Analysis

The following material properties are assumed for the filament.

Property	Abbr.	value
Elastic Modulus	E	2,3 GPa
Yield Strength	$R_e$	26,4 MPa
Tensile Strength	$R_m$	35,9 MPa
Density	$\rho$	1,25 g/cm <sup>3</sup>

Table 23: Properties of PLA [11]

Additionally to the design Factor of Safety  $FOS_d = 1,2$  a 3D Printing Factor of Safety  $FOS_{3dp} = 2$  is used ( $FOS = FOS_d \cdot FOS_{3dp}$ ). This factor covers the uncertainties for the anisotropic behavior of 3D prints. A minimal thickness of  $t_{min} = 2$  mm is also assumed, as the anisotropic behavior for walls thinner than  $t_{min}$  is assumed to be much higher than it is covered by the Factor of Safety. An experiment to validate the Factor of Safeties and the calculations shall be made (see chapter 6.1).

The link can fail due to three criteria. Material failure  $\sigma_{design} > \sigma_{limit}$ , deformation  $f_{design} > f_{limit}$  or buckling  $F_{design} > F_{Buckle}$ .

The material failure is defined by the 2<sup>nd</sup> moment of area, the section modulus and the occurring moments. The cross section analysis is done for an I beam and a tube.

Profile	$I_y$	$I_z$	$I_t$	$W_{by}$	$W_{bz}$	$W_t$
Tube	$I_b = \frac{\pi}{4}(R^4 - r^4)$		$I_t = \frac{\pi}{2}(R^4 - r^4)$	$\frac{I_b}{R}$	$\frac{I_t}{R}$	
I beam	$\frac{BH^3 - bh^3}{12}$	$\frac{HB^3 - hb^3}{12}$	$\frac{1,31}{3} \sum h_i t_i^3$	$\frac{2I_y}{H}$	$\frac{2I_z}{B}$	$\frac{I_t}{t_{max}}$

Table 24: 2nd moment of area and section modulus for different cross section profiles

where,  $R$  outer Radius,  $r$  inner Radius. For ductile materials the general plane stress state of the *van Mises yield criterion* can be assumed.

$$\sigma_v = \sqrt{\sigma_{by}^2 + \sigma_{bz}^2 - \sigma_{by}\sigma_{bz} + 3\tau^2}, \quad \sigma_v \stackrel{!}{\leq} \frac{R_e}{FOS} \quad (58)$$

where

$$\sigma_{by} = \frac{M_y}{W_{by}}, \quad \sigma_{bz} = \frac{M_z}{W_{bz}}, \quad \tau = \frac{M_t}{W_t} \quad (59)$$

The deformation is characterized by the 2<sup>nd</sup> moment of area, the bending moment and the Elastic modulus.

$$f = \frac{M_b l^2}{2EI_b} \stackrel{!}{\leq} f_{max} \quad (60)$$

The critical buckling force is dependent on the bounding conditions and the worst case (Eulerfall 1, ref. Figure 17) is assumed for this case.

$$F_{buckle} = \frac{\pi^2}{4} \frac{EI_{b,min}}{l^2}, \quad FOS \stackrel{!}{\geq} \frac{F_{buckle}}{F_{design}} \quad (61)$$

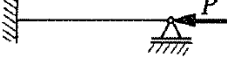
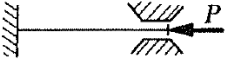
Eulerfall	Systemskizze	kritische Last
1		$P_{krit} = \frac{\pi^2}{4} \frac{EJ_y}{l^2}$
2		$P_{krit} = \pi^2 \frac{EJ_y}{l^2}$
3		$P_{krit} = 2,046 \pi^2 \frac{EJ_y}{l^2}$
4		$P_{krit} = 4 \pi^2 \frac{EJ_y}{l^2}$

Figure 17: Critical Buckling force [12]

The paver design allows the arm to have a total inaccuracy of about 10 mm. The tolerances of each joint can therefore be  $\pm 1$  mm. To cover additional slack in the joints a maximum deformation of the links  $f_{max} = 0,5$  mm is allowed. *MATLAB* calculates the minimal cross section areas while satisfying the above criteria. For all cross sections, the deciding criteria is the maximum deformation. (units: area A in [ $mm^2$ ], mass m in [ $kg$ ], rest in [ $mm$ ]).

Link	A	m	B	H	tb	th
2	755,5	0,212	60,0	60,0	6,7	3,3
3	389,1	0,109	60,0	60,0	2,4	2,1

Table 25: Cross Section Areas I Beam

Link	A	m	R	t
2	814,5	0,229	30,0	4,7
3	427,9	0,120	30,0	2,4

Table 26: Cross Section Areas Tube

The moment reduces over the length of the links (ref. Figure 18). Therefore the cross section can vary of the length as well. Figure 19 shows the cross section at the beginning (solid line) and at the end of the link (dotted line).

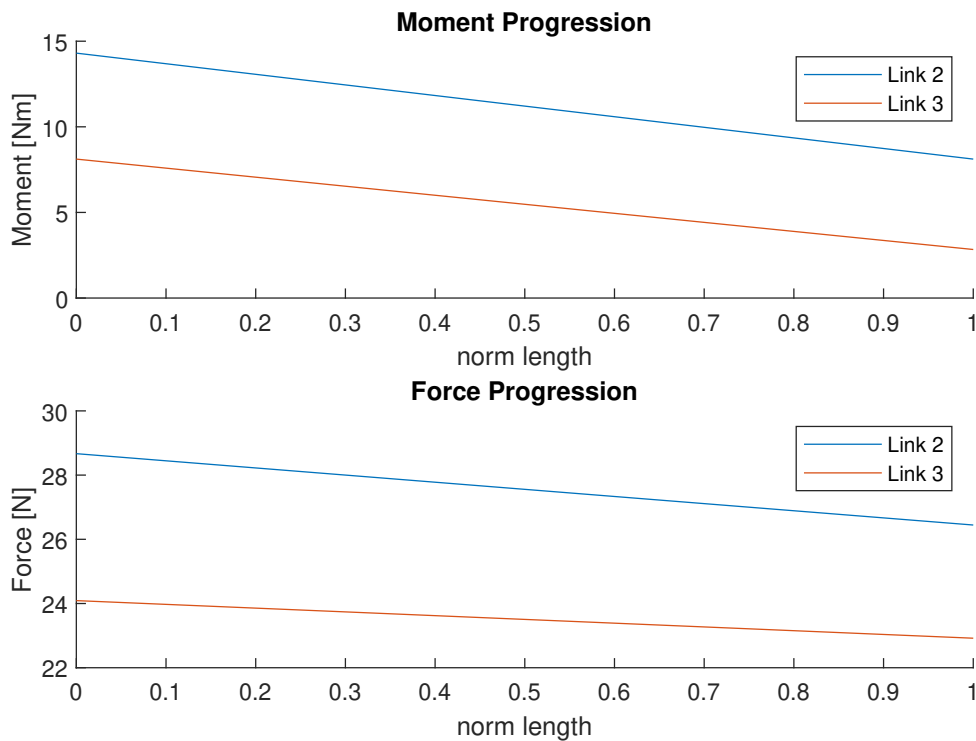


Figure 18: Moment/Force Progression over the length of link 2 and 3

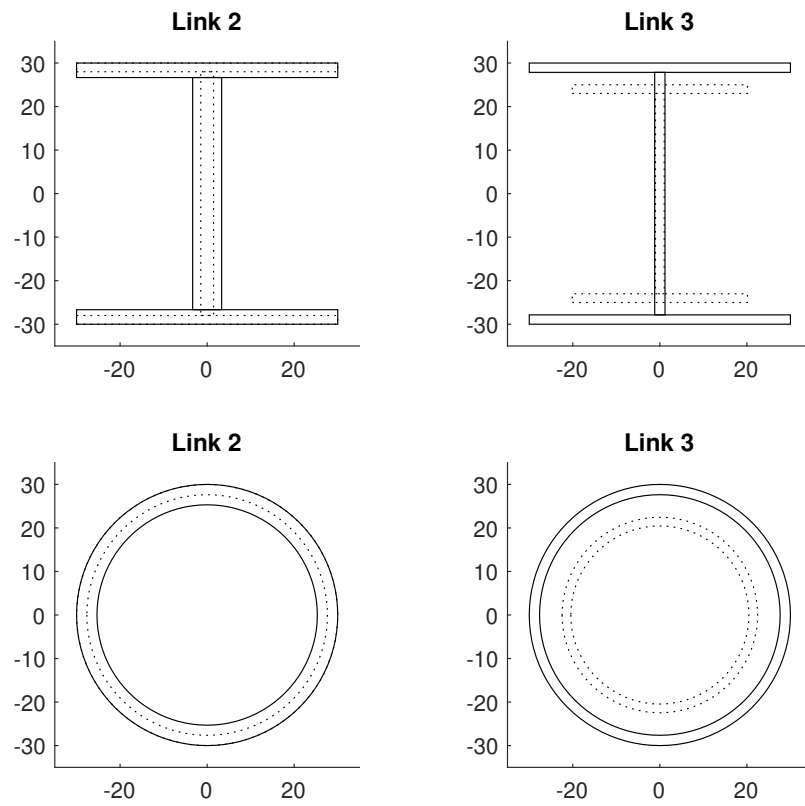
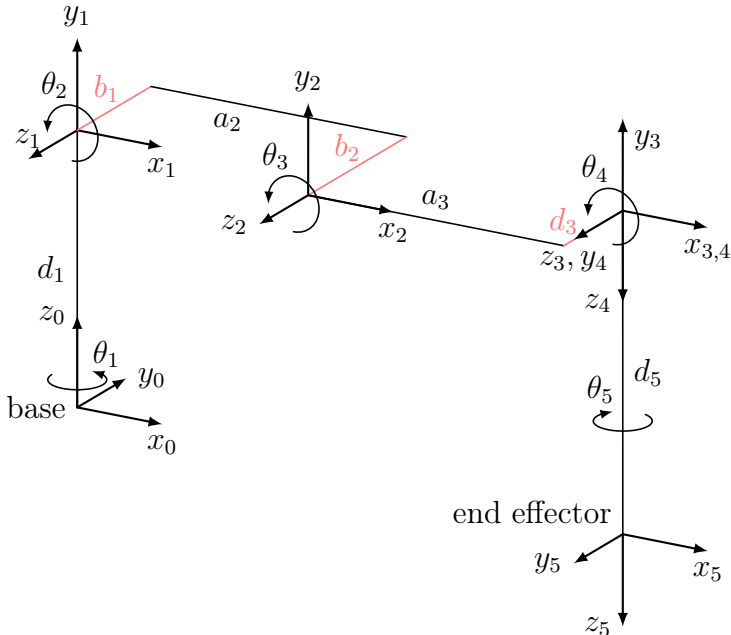


Figure 19: Cross Sections for different Profiles

To improve 3D printability the taper is not included in the final design.

## 4.7 Third Iteration

During the design process it became clear, that an arm without additional offsets (ref. Figure 14) cannot be designed. The more sophisticated design (ref. subsection 5.2) defined these new offset parameters, as well as the minimum length of the links 1, 4 and 5.



Frame No.	$\theta$	$\alpha$	a	d
1	$\theta_1$	90°	0	$d_1$
2	$\theta_2$	0	$a_2$	$b_1 - b_2$
3	$\theta_3$	0	$a_3$	$d_3$
4	$\theta_4$	90°	0	0
5	$\theta_5$	0	0	$d_5$

Table 27: DH parameters with offsets

Figure 20: Coordinate Frames with offsets for DH Parameters

The lengths of link 2 and 3 ( $a_2, a_3$ ) are recalculated in MATLAB in order to minimize the total length in regard to the newly set parameters. The total length was reduced from 676,1 mm to 662,7 mm.

Link	$L_1$	$L_2$	$L_3$	$L_4$	$L_5$
Length in [mm]	117,0	220,3	220,3	71,0	34,0

Table 28: Link lengths for the third iteration

The designs of the Strain Waves made clear, that the lower the transmission requirement, the better a 3D printing approach is suited. So far the required transmission ratio was deduced with the worst static scenario with the arm in the *Stretched Configuration*. As this is the theoretically worst case scenario with the highest loads on the links and the joints, it can be avoided with a software implementation with soft limits. Therefore the *Standard Configuration* is now seen as the new worst static scenario. In the exemplary unloading sequence (Figure 21) it can be seen, that the operating range of the arm is always inside of the spanned range of the *Standard Configuration* which is displayed in blue.

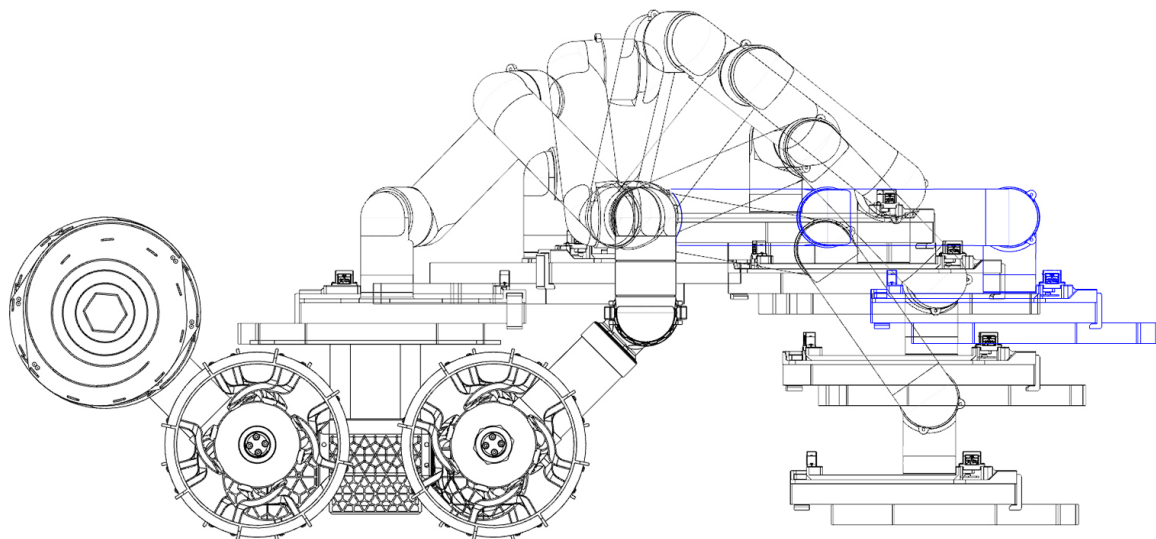


Figure 21: Unloading Sequence with Standard Configuration

The resulting reduction of the joint torques due to this decision are displayed in the following table.

Joint	Torque [Nm]		Transmission ratio		Reduction
	from	to	from	to	
1	15,4	12,2	36,8	29,1	21%
2	15,4	12,2	36,8	29,1	21%
3	8,7	5,6	20,8	13,4	35%
4	3,0	0,0	7,1	0,0	100%
5	2,9	0,0	7,0	0,0	100%

Table 29: Reduction of the joint torques

The tests (ref. chapter 6.1) showed, that the assumption to use the yield strength  $R_m$  of PLA cannot be made and that the strength is highly filament dependent. For safety the lowest value  $\tau = 3 \text{ Nmm}$  is used and the new thicknesses of the links are calculated.

Link	A	m	R	t
2	746,7	0,206	30,0	4,3
3	406,8	0,112	30,0	2,2

Table 30: Cross Section Areas Tube Profile for the third iteration

Even though the bearable strain was reduced, the required thickness was reduced for both links for about 0,1 mm. As shown in the second iteration the dimensioning criteria is the allowed deformation and not the bearable strain. Additionally the occurring load was reduced which also resulted in a thinner wall requirement.

## 4.8 Final Iteration

The final design of the arm requires the implementation of cycloidal drives. The designed transmissions come with a specific weight, which need to be considered in the torque analysis. So far the preceding torque analyses made use of an preliminary weight distribution of the links as well as a smaller motor weight. Including all these new parameters, the final torque analysis results in the following table. It has to be noted, that the required torque from joint 1 results from the assumed deceleration  $\ddot{\theta}_1$  and can be significantly be reduced by a slower movement of the arm. Joint 2 in contrary is defined by the load at the end-effector and needs to be achieved via the transmission in order to guaranty the functionality of the arm.

Joint	Torque [Nm]		Transmission ratio		Increase
	from	to	from	to	
1	12,2	14,7	29,1	32,7	12%
2	12,2	14,3	29,1	31,8	9%
3	5,6	6,6	13,4	14,4	8%
4	0,0	0,0	0,0	0,0	0%
5	0,0	0,0	0,0	0,0	0%

Table 31: Increase of the joint torques

The required thicknesses of Link 2 and 3 changed to:

Link	A	m	R	t
2	642,5	0,25	38,0	2,8
3	463,4	0,16	33,0	2,0

Table 32: Cross Section Areas Tube Profile for the final iteration

The selected bearing needs to be able to transmit the moments around the non rotating axis. The permissible moment load can be determined with<sup>3</sup>:

$$M_{perm} = 0,23 \cdot d_1 \cdot \left( \frac{C_{0a}}{s_0} - F_a \right) \quad (62)$$

, where  $d_1$  is the outside diameter of the inner ring,  $C_{0a}$  is the basic static load rating of the thrust roller set,  $s_0$  is the safety factor<sup>4</sup> and  $F_a$  is the acting axial load. For the selected Bearing (61807) the permissible moment load is determined according to the datasheet (Appendix B).

$$M_{perm} = 0,23 \cdot 38,21 \text{ mm} \cdot \left( \frac{3,35 \text{ kN}}{4} - 0,042 \text{ kN} \right) = 6,98 \text{ Nm} \quad (63)$$

<sup>3</sup>SKF Loads, <https://www.skf.com/group/products/super-precision-bearings/axial-radial-crb/loads> (accessed: 22.02.2020)

<sup>4</sup>SKF Bearing size, <https://www.skf.com/group/products/super-precision-bearings/principles/bearing-selection-process/bearing-size> (accessed: 22.02.2020)

Table 33 shows the permissible moment load in the stationary case. It can be seen that for all joints, the occurring moments are always lesser than the permissible load.

Joint	$F_a[N]$	$M_{perm}[Nm]$	$M_x[Nm]$	$M_y[Nm]$
1	42,87	6,98	2,18	0
2	0	7,36	2,18	0
3	0	7,36	2,27	0
4	0	7,36	0	0
5	0	7,36	0	0

Table 33: Permissible moment load, stationary

When a decelerating case is applied (e.g.  $\ddot{\theta}_1 = 0,16 \frac{\text{°}}{\text{s}^2}$ ), the occurring moments of joint 1 and 2 exceed the permissible moment load (ref. Table 34).

Joint	$F_a[N]$	$M_{perm}[Nm]$	$M_x[Nm]$	$M_y[Nm]$
1	42,87	6,98	0,06	7,88
2	22,91	7,16	7,88	2,74
3	18,77	7,20	3,31	2,83
4	1,48	7,35	-0,09	0
5	0,57	7,36	-0,06	0

Table 34: Permissible moment load, dynamic/decelerating

The chosen bearings therefore are limiting the movement speed of the arm. For higher movement speeds, angular contact bearings can be used, but the controlling software nonetheless needs to be aware of this limiting factor.

## 5 Design

### 5.1 Transmission

The torque requirement of 14 Nm as calculated in chapter 4 can not be satisfied with a conventional Stepper Motor without making use of a transmission. Rather than purchasing an existing transmission, it was decided to design a 3D printable transmission that is geared to the specific needs of the arm.

#### 5.1.1 Strain Wave Gear

Table 5 shows that either planetary gears or harmonic drives were used in these rover arms, whereas the *dexterous robot arm* as the newest design uses an harmonic drive which is a strain wave gear. The harmonic drive was firstly patented in 1964<sup>5</sup> and already used in 1971 on the Apollo Lunar Roving Vehicle<sup>6</sup>. This and the use in the listed rover arms show that the harmonic drive is suited for the use in space and is inspected for use in this arm.

A strain wave gear consists of three main components, the wave generator, the flex spline and the circular spline. The elliptical wave generator elastically deforms the flex spline that has teeth arranged on the outer circumference. The rigid circular spline displays matching but more (2 in general) teeth on the inner circumference. This design results in multiple advantages [13]:

- no backlash and no backdrivability
- light weight with high compactness
- high gear ratios
- excellent repeatability
- excellent position accuracy
- possible hollow shaft for cable routing

Especially the non-backdrivability and the high compactness make it an ideal gearing mechanism for robot arms. The reduction ratio of this gearing mechanism is determined with the teeth count:

$$\text{reduction ratio} = \frac{\text{flex spline teeth} - \text{circular spline teeth}}{\text{flex spline teeth}} \quad (64)$$

where the flex spline teeth is two less than the circular spline teeth.

#### 5.1.2 Design of the Strain Wave Gear

Two different designs are investigated further. The first design is inspired by the *How to mechatronics* user *Dejan* [14] and the second one by *Simon Merret's* strain wave gear with timing belt design [15], where the main difference is the flexible part. *Dejan* uses an all printed approach whereas *Simon Merret* uses a timing belt for the flexible part.

<sup>5</sup>US3214999A, <https://patents.google.com/patent/US3214999A/en> (accessed: 28.01.2021)

<sup>6</sup>The Apollo Lunar Roving Vehicle, [https://nssdc.gsfc.nasa.gov/planetary/lunar/apollo\\_lrv.html](https://nssdc.gsfc.nasa.gov/planetary/lunar/apollo_lrv.html) (accessed: 28.01.2021)

The following motors were considered:

Nr	1	2	3	4	5	6	7	8
Type	Nema 14		Nema 16		Nema 17		Nema 23	
Torque [Nm]	0,23	0,4	0,21	0,25	0,26	0,45	0,55	0,6
Mass [kg]	0,22	0,35	0,19	0,27	0,23	0,28	0,47	0,5
width [mm]	35		39		42		57	
height [mm]	35		39		42		57	
length [mm]	42	52	34	44	34	39	41	42
Torque/Mass ratio	1,05	1,14	1,11	0,93	1,13	1,61	1,17	1,20

Table 35: Considered Motors for Transmission Calculation [16]

Each motor needs a distinct reduction ratio that is indirect proportional to the required diameter of the gears. In this range a timing belt with a module of 3 mm is suitable and the belt length is given by the circular spline teeth. For the design of *Dejan* the module and pitch is calculated with a given diameter. This diameter is selected in the same order of magnitude as the motor, making the overall transmission system compact.

Nr.	1	2	3	4	5	6	7	8
reduction ratio	0,016	0,029	0,015	0,018	0,019	0,032	0,039	0,043
Flex Spline Teeth	122	70	134	112	108	63	51	47
Circular Spline Teeth	124	72	136	114	110	65	53	49
Belt Length [mm]	366	210	402	336	324	189	153	141
Belt Diameter [mm]	116,5	66,8	128,0	107,0	103,1	60,2	48,7	44,9
diameter [mm]	35	35	39	39	42	42	57	57
module [mm]	0,29	0,50	0,29	0,35	0,39	0,67	1,12	1,21
P [mm]	0,90	1,57	0,91	1,09	1,22	2,09	3,51	3,81

Table 36: Strain Wave Parameters for each Motor

Table 36 displays that the motors 1-5 all require a low reduction ratio and therefore a large number of teeth. This results in a large belt length and a small module. Simple 3D printing technologies are limited in their accuracy and the smaller the module, the higher are requirements on the accuracy. With the standard accuracy of a 3D printer that ranges from 0,1 mm to 0,4 mm a minimum module of 1 mm is advised. These are achieved for the motors 7-8 but as these are large and heavy motors, and the torque to mass ratio is worse than for motor 6, which is chosen for the next design steps. The module is presumed with 1 mm which results in a larger diameter that is still in an acceptable range.

With these dimensions first draft designs were made.

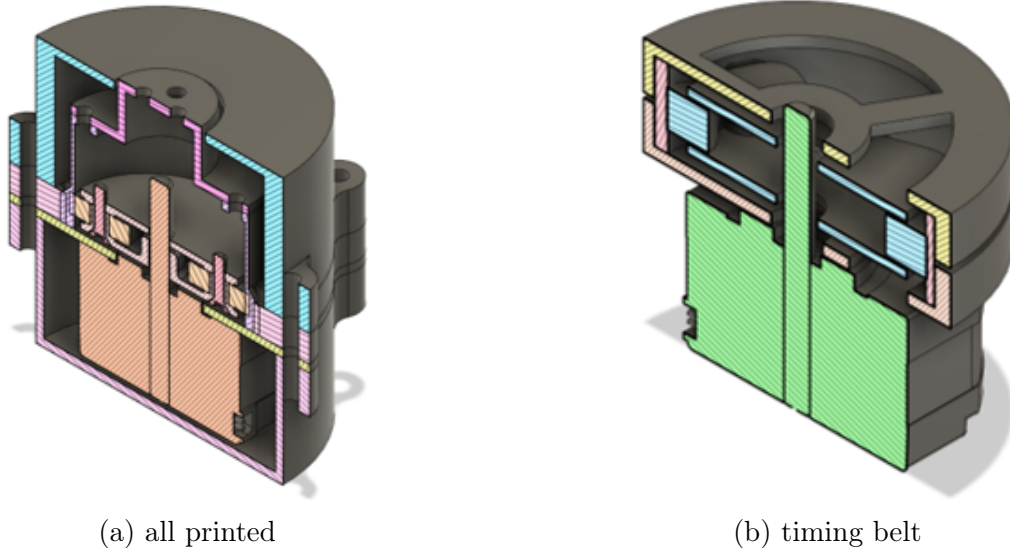


Figure 22: First draft designs of the different transmission designs

### All printed design

The all printed design is worth striving for as it limits the amount of bought-in parts to just the bearings. As explained above, the user *Dejan* managed to design a working prototype and the adapted design is showed below.

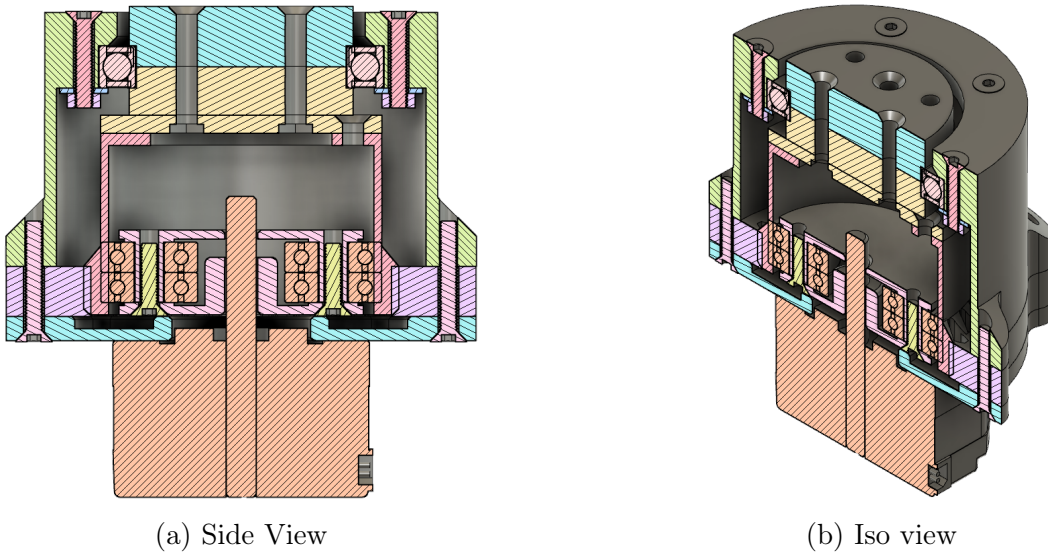
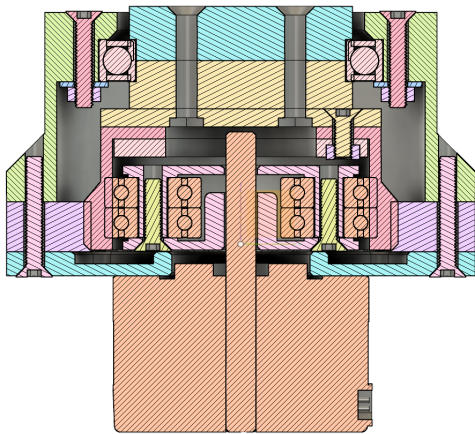


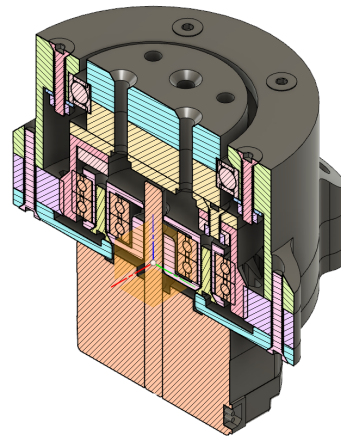
Figure 23: All printed PLA Strain Wave Gear

This design worked for a short amount of time, but then the flex spline broke as the brittle PLA could not handle the flexing and the applied torsion. The material tests (see cha. 6.1) and the followed calculations determined the thickness of the flex spline to  $t = 1,3 \text{ mm}$ . With this thickness the flex spline is no longer flexible enough to fulfill its part. The design could not be tested and is neglected from now on.

Thermoplastic polyurethane (TPU) filament is a flexible filament which was also tested in the all printed design. It can be seen that the major difference is the reduced height. The TPU is too flexible and is also disregarded (ref. cha. 6.4).



(a) Side View

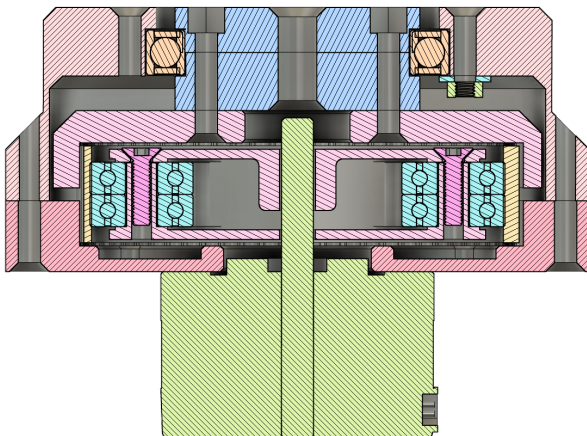


(b) Iso view

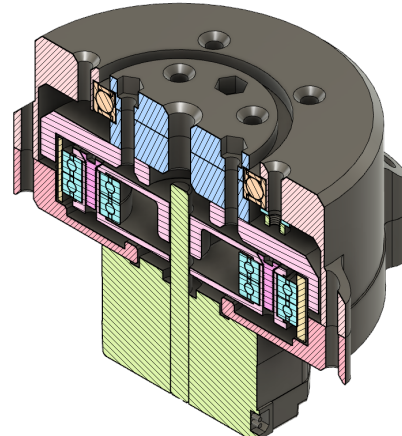
Figure 24: All printed TPU Strain Wave Gear

### Timing belt design

The timing belt design from *Simon Merret* is adapted to the needs of the project. The design is lower in height but used a larger outer diameter. The test results were promising but the soft timing belt limited the final transmission ratio (ref. cha. 6.4).



(a) Side View



(b) Iso view

Figure 25: Strain Wave Gear with Timing Belt

### 5.1.3 Cycloidal Drive

The 3D printed strain wave designs seem to be limited in the achievable transmission ratio by the properties of the filament and the timing belt. A possible iteration step could be the investigation into a larger module timing belt that would have further increased the outer diameter of the transmission or different filaments (e.g. Nylon). It is decided that another design might be better suited for 3D printing and the cycloidal drive is seen promising.

A cycloidal drive consists of four main components which are shown in the figure below, the pins in the frame (grey), the eccentric shaft (green), the cycloidal discs (blue) and the output shaft (red). The cycloidal discs are driven by the eccentric shaft (sometimes eccentric bearings) and roll over the pins of the rigid frame. This rolling of the pins determines the shape of the cycloidal discs. The Output Shaft rotates freely inside the holes of the cycloidal disc to remove the eccentricity.

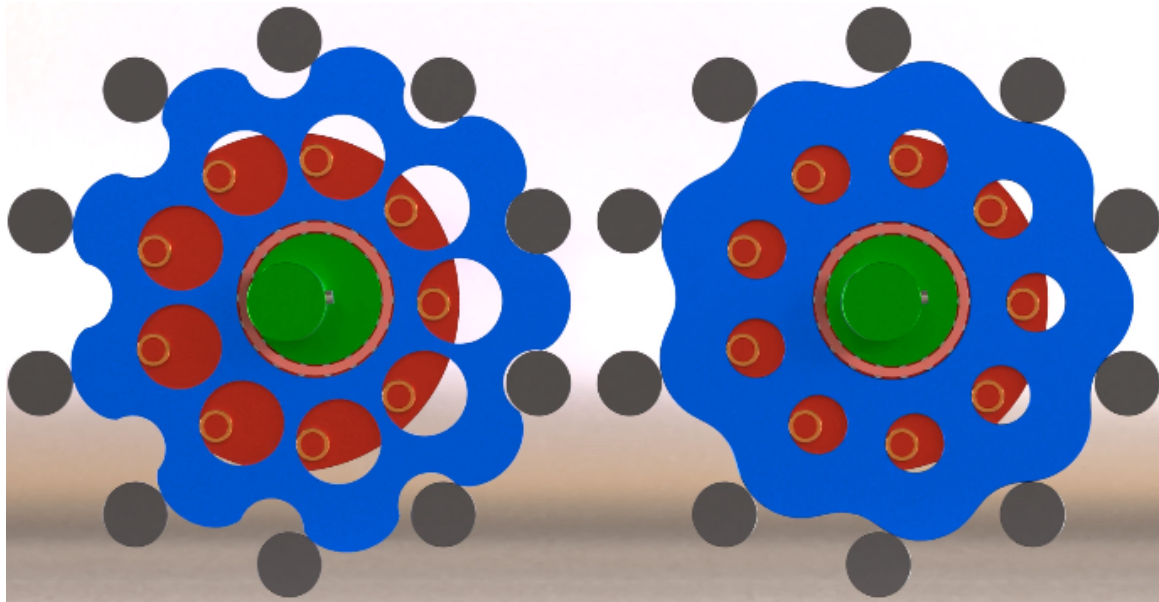


Figure 26: Ordinary cycloidal Drive (left). Cycloidal drive with contracted cycloid disc (right) [17]

Figure 26 also shows a cycloidal disc which was designed with a contracted cycloid. With this design the eccentricity is reduced in order to reduce the vibrations at high rotation speeds and in this case to improve the 3D printability. The advantages of this gearing mechanism are:

- no backlash
- high gear ratios
- light weight with high compactness
- high contact areas at the teeth

The advantages are similar to the harmonic drive, but the cycloidal drive is backdrivable. In the case of a robotic arm it means, that the motors must remain holding torque or that an additional brake must be implemented. This results in higher power needs and/or additional weight due to the implementation of brakes. For this design it is assumed that the power supply is given and no additional brake is needed.

### 5.1.4 Design of the Cycloidal Drive

The first design is made with 5 mm pins, a low reduction ratio and with ordinary cycloidal discs. Over the next design it could be seen that the use of a contracted cycloid ( $0,8 \cdot r$ ) improved the 3d printability. The use of an end plate and screws with spacers allowed to enclose the cycloidal discs and improve stability and the resulting transformation ratio.

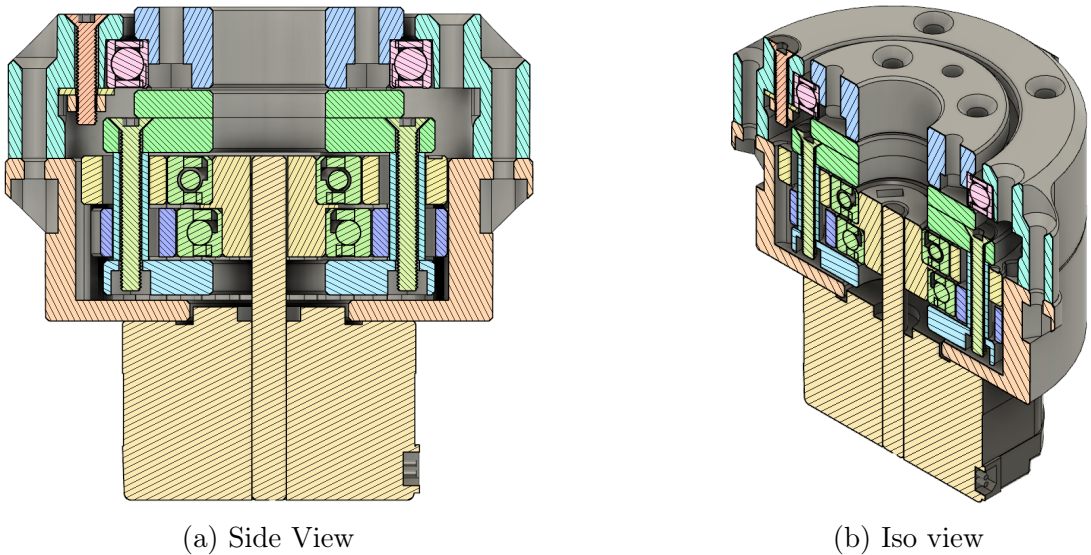


Figure 27: Cycloidal Drive

The required transmission ratios vary between approximately between 13 and 30 and it makes sense to make two individual transmissions. The first transmission is set to a reduction ratio of 30:1 and the outer diameter roughly sized to fit to the diameter of the links. Chapter 6.4 shows, that this design produces a reduction ratio of 22:1 which calculates to 74% of the theoretical value.

Figure 28 shows an explosion view of the cycloidal drive. The output shaft (red) is assembled at first with the cycloidal discs (blue) and the eccentric shaft (yellow) in between. This sub-assembly is connected to the hull (green, right) and then slid into the frame (green, left). This assembly is then mounted to the corresponding link. The hull has a trigger which is specifically designed for each endstop of the corresponding joint.

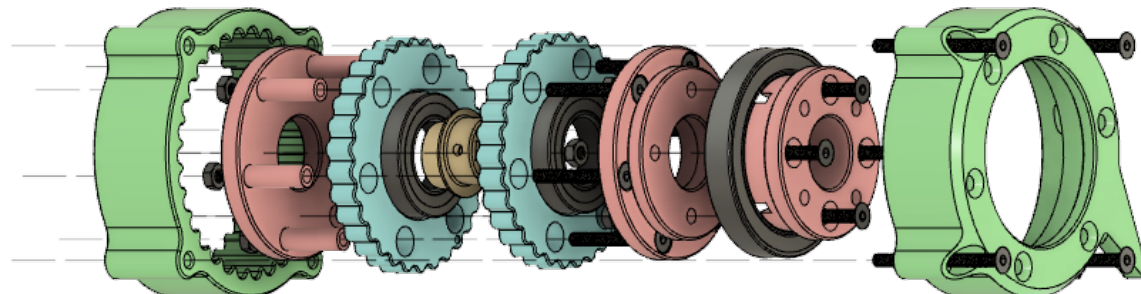


Figure 28: Explosion view of the Cycloidal Drive

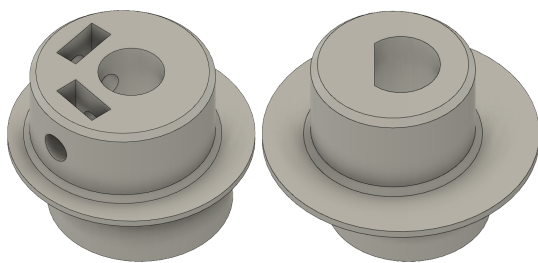


Figure 29: Eccentric Shaft design change

At first it was planned to tighten the eccentric shaft to the output shaft of the stepper motor via grub screws. During later designs, the grub screws are left out and an inner contour of the eccentric bearing which fits the contour of the shaft of the motor is used. No slipping is noticed at this contact point. During long time usage, this is most likely the first part which plastically deforms and needs changing.

## 5.2 Design of the Links of the Arm

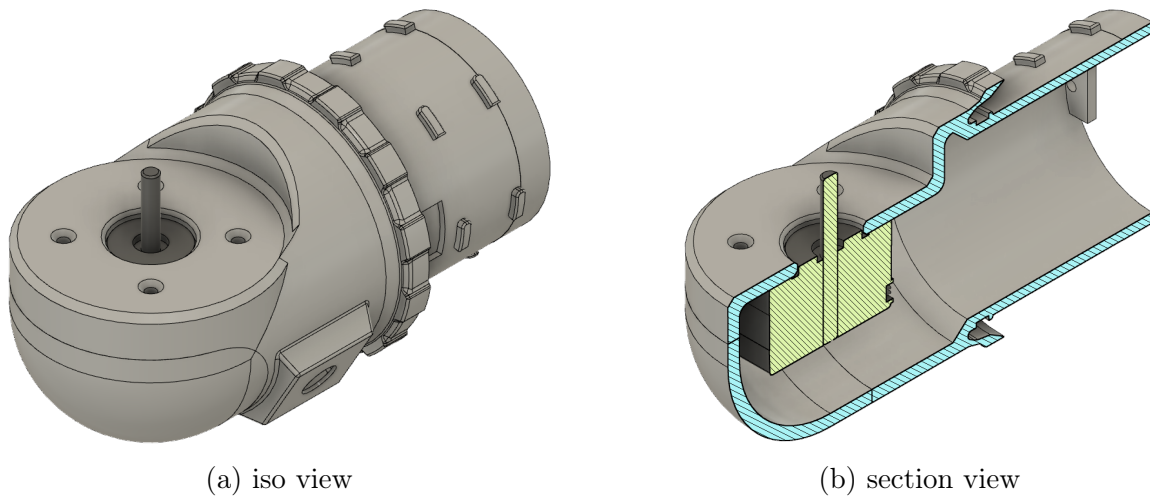


Figure 30: Attachment Part Design

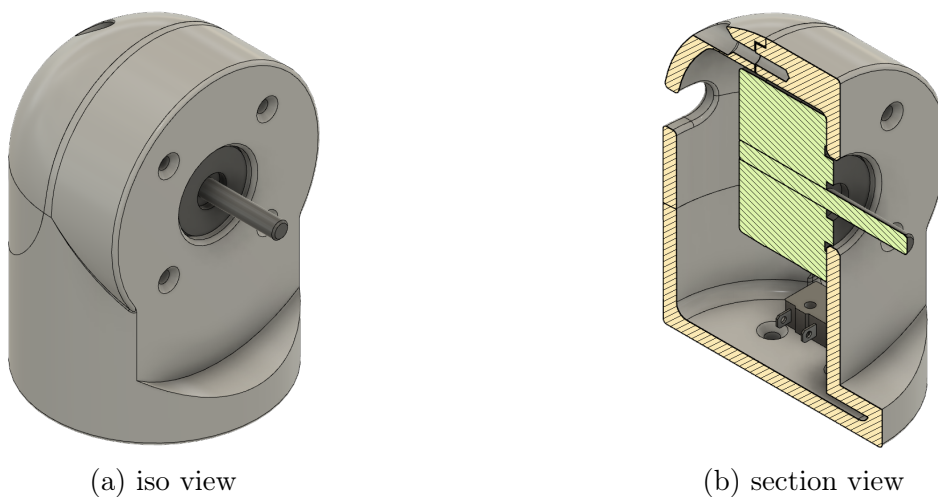


Figure 31: Link 1 Design

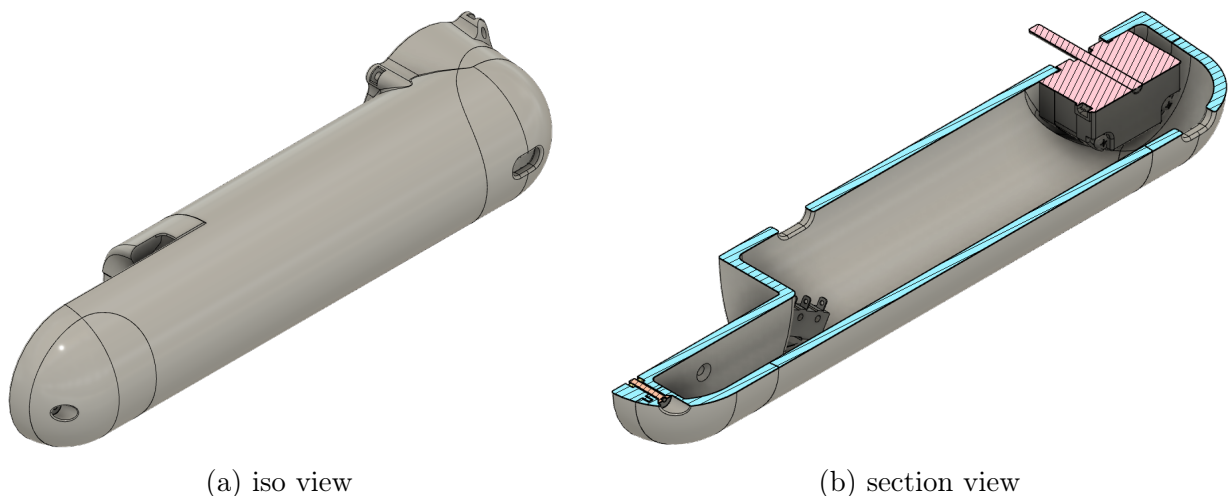


Figure 32: Link 2 and 3 Design

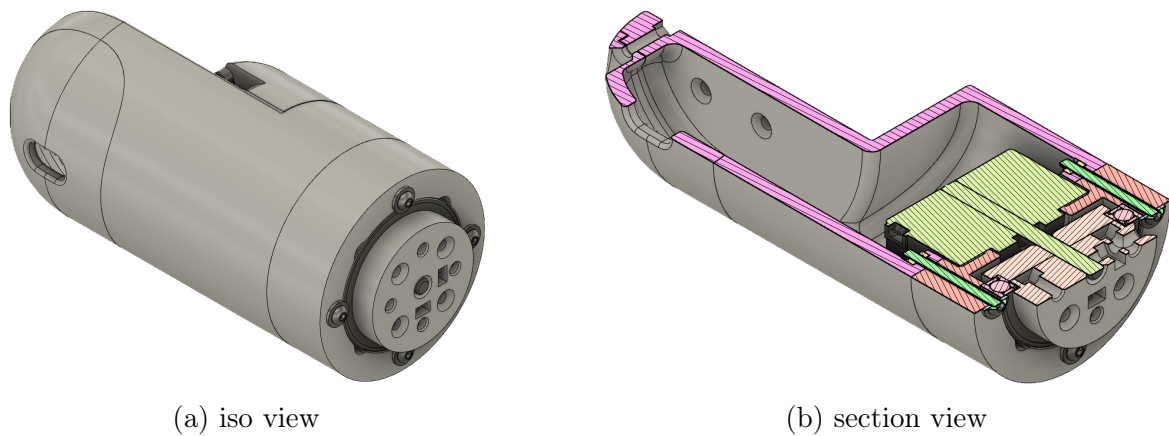


Figure 33: Link 4/5 Design

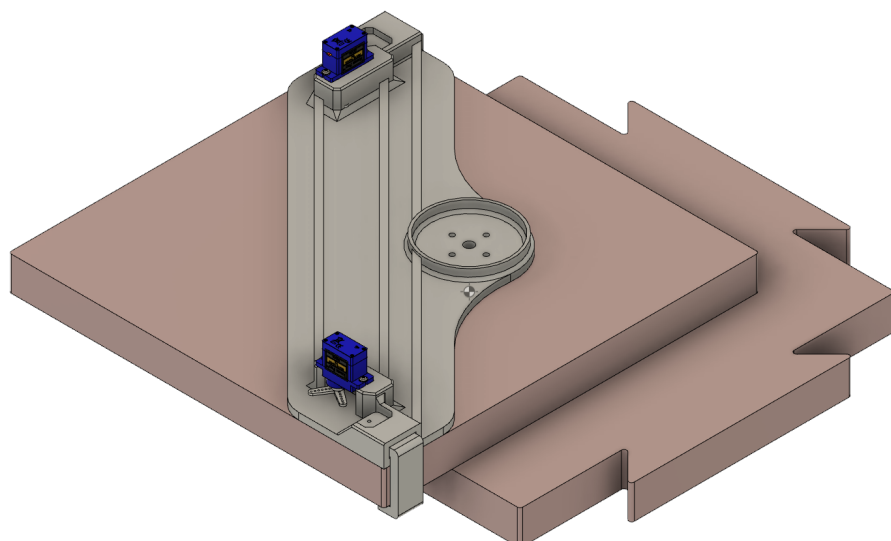


Figure 34: End Effector Design

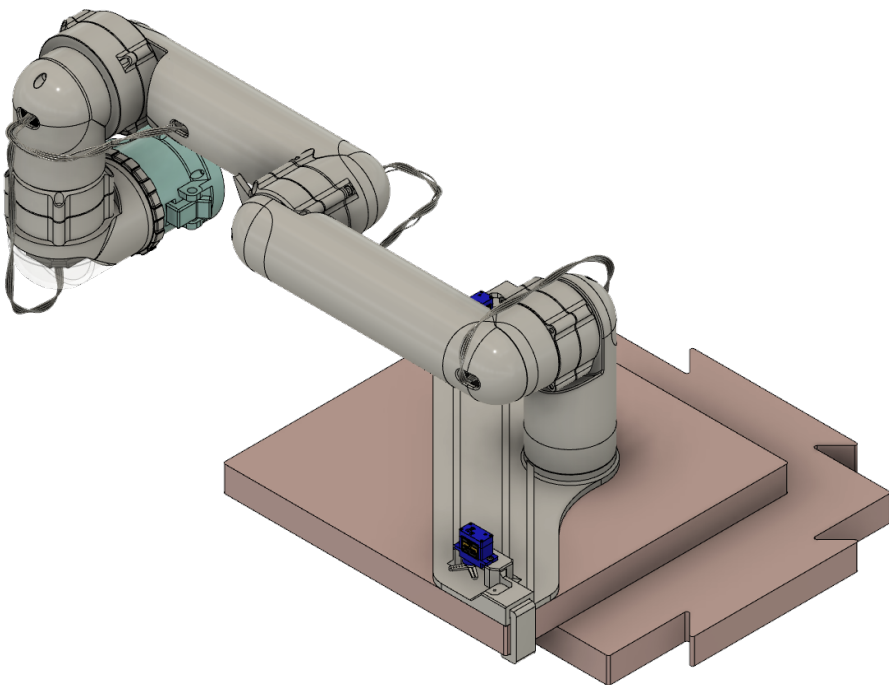


Figure 35: Complete Arm Design

## 6 Testing

### 6.1 Material Properties of 3D printed PLA

The material properties of a 3D print are not researched in great detail, therefore the properties of pure PLA [11] are assumed. To verify these properties as torsion test is conducted. Figure 36 shows the test setup for the Torsion test.



Figure 36: Test Setup for Torsion PLA Test

A controlled force is applied and measured at the end of the lever. This force is then converted into the resulting torque at the test sample. With the wall thickness the occurring torsional stress  $\tau$  is calculated. Two tests with different thicknesses were conducted.

Test Nr.	max. load [kg]	max. Torque [Nmm]	Radius [mm]	Wall thickness [mm]	$\tau$ [Nmm]
1	4,50	11522	35	0,48	3,2
2	8,25	21123	35	0,96	3,0
3	8,25	21123	35	0,48	5,8
4	10,00	25604	35	0,48	7,1
5	9,50	24324	35	0,48	6,7

Table 37: Torsion Test Results

It can clearly be seen, that the bearable strain is notably less than the currently assumed Yield Strength  $R_e = 26,4 \text{ Nmm}$ .

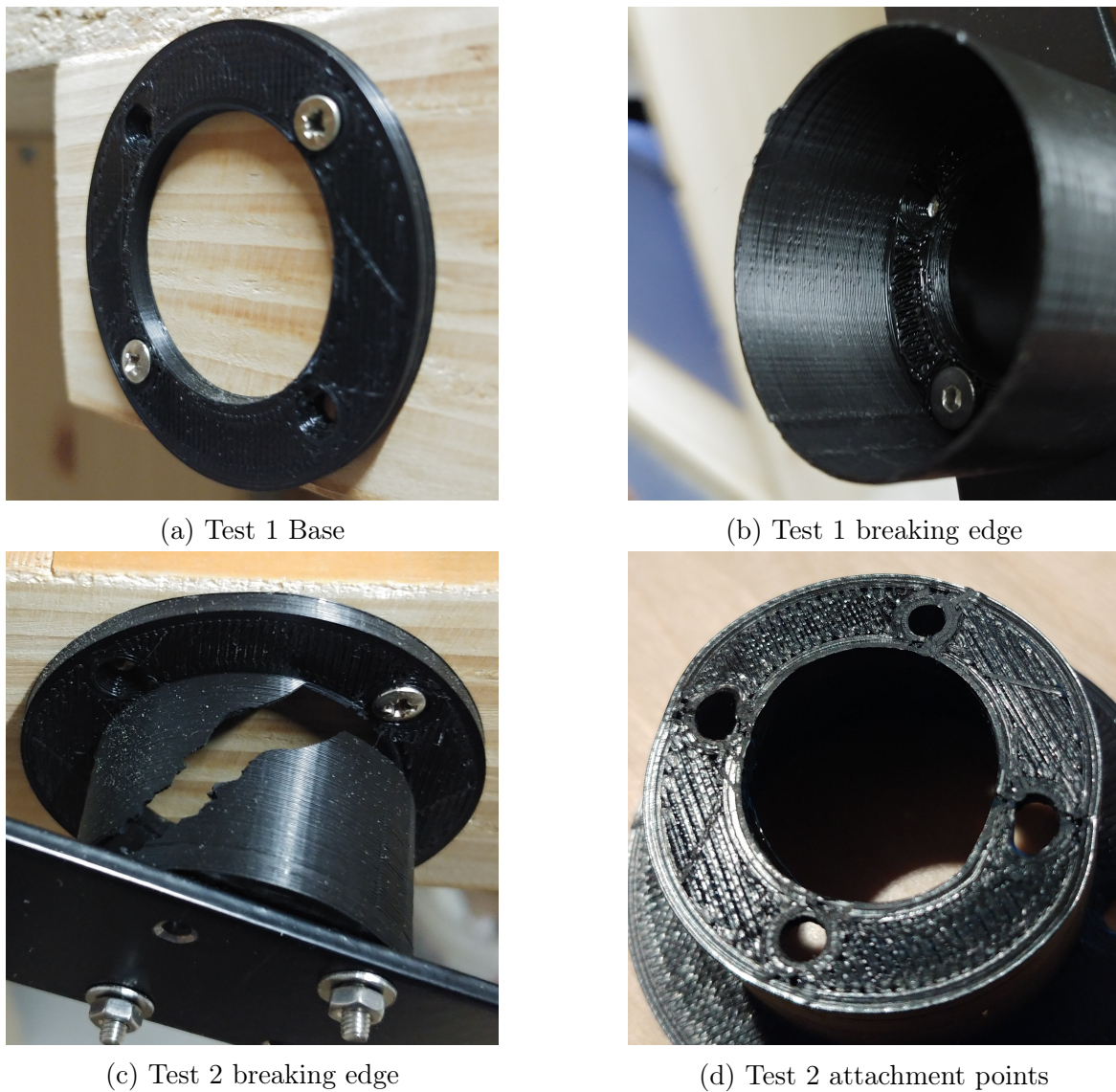


Figure 37: Pictures of Torsion Test specimen Black PLA

Figure 37b displays a clean breaking edge of the specimen, which is untypical for a torsion test. It is assumed that at this test the layer adhesion of the single wall extrusion is the restricting factor. This assumption is strengthened as the second test with a double wall thickness does not display this behavior. Instead it shows the typical screw type shear (ref. Figure 37c) which is to be expected at a torsional test. The second also shows a deformation at the application of force. This shows that the bearing pressure is too high at this load and resulted in creeping of the PLA. One can either increase the thickness of the mounting plate or increase the number of attachment points/holes.

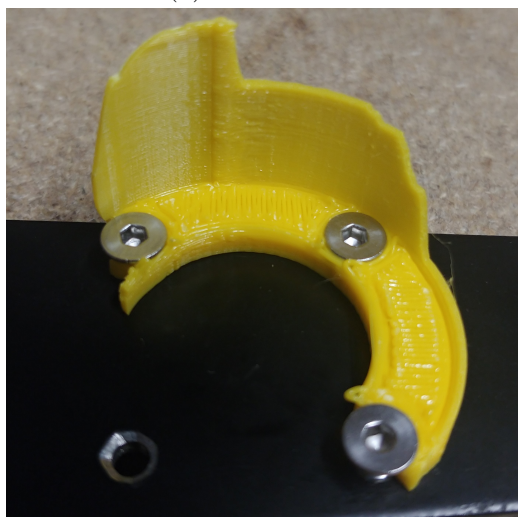
Tests with a different PLA showed similar but much higher results. The increased thickness at the mount of the lever eliminated the problem of the too high bearing pressure. The first test showed the same shearing as the first test with the black PLA. The second and third test however did not fail due to shearing but through torsion even though the wall thickness has not been increased, which shows the inaccuracy and unpredictability of 3D printed parts.



(a) Test 1 Base



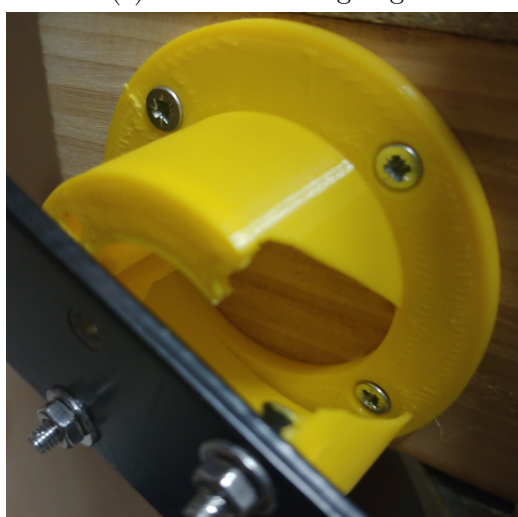
(b) Test 1 breaking edge



(c) Test 2 breaking edge



(d) Test 2 attachment points



(e) Test 2 breaking edge



(f) Test 2 attachment points

Figure 38: Pictures of Torsion Test specimen Yellow PLA

## 6.2 Software

The first controlling of the stepper motor is achieved with a 3D printer mainboard. Due to the current limitation, new dedicated controlling hardware and software is used, after the first torque tests of the motor. The existing stepper motors inside the RASSOR are controlled via an Microcontroller<sup>7</sup> with an attached motor driver shield<sup>8</sup>. To ensure a smooth integration of the arm the same hardware is used for the motors of the arm.

For testing purposes a simple Arduino Sketch is written and the provided libraries of the stepper are used wherever possible to allow for precise and/or strong stepper movement. The provided libraries include different steptypes which each comes with different advantages and disadvantages. The *Single* and *Double* steptype stand for single or double coil activation respectively. While providing more torque the movement is hard and the minimum rotation speed relatively high. This results in an oscillation at the end of the torque lever whenever a position is reached. As opposed to this the *Microstepping* method creates a smooth motion while still providing enough torque.

With this sketch the motor can be controlled via commands sent over the Serial Communication. The commands consist of two chars and an integer. The first char specifies the command type ('m' for settings, 'g' for movement without transmission, 't' for movement with strain wave transmission, 'c' for cycloidal drive transmission). The following char and integer specify the parameters passed with the command type. The following commands are integrated into the software while only pressing *Enter* the last command will be repeated:

Type	Parameter		Description
M	S	rpm	Set the speed of the motor in rpm
	N	tr	Set the transmission ratio
	T	1-4	Set the steptype of the motor. Single(1), Double(2), Interleave(3), Microstepping(4)
	P		Display the current position in steps and degree
	Z		Set the current position as 0
	C		Display the current configuration (speed, transmission ratio, steptype)
	R		Release the motor to move freely
G/T/C	F	steps	Forward/Clockwise movement in steps
	B		Backward/Anticlockwise movement in steps
	M		Move to the specified position (steps)

Table 38: Serial Commands to control the Stepper Motor

<sup>7</sup>Arduino MEGA 2560, <https://store.arduino.cc/arduino-mega-2560-rev3> (visited: 06.01.2021)

<sup>8</sup>Adafruit Stepper Shield V2.3, <https://www.adafruit.com/product/1438> (visited: 06.01.2021)

### 6.3 Propagation of uncertainty

During experimental measurements each variable brings along its uncertainty e.g. the precision of a scale. These uncertainty propagate due to the combination the variables in order to get a final result of the experiment. With a *propagation of uncertainty* or *error propagation* this final uncertainty can be determined in order to evaluate the final result.

The first tests which were conducted without a force scale (ref. chapter 6) no error propagation was done. The new test setup displayed multiple variables ( $m$ ,  $\alpha$ ,  $l$ ) with a high uncertainty, especially the force scale, which required an error propagation. To calculate the transmission ratio with the tested force read from the force scale following equation is used:

$$r = \frac{\cos \alpha \cdot mg \cdot l}{M_0} \quad (65)$$

, where  $g$  is the earths gravity  $g = 9,81 \text{ m/s}^2$  and  $M_0$  the torque of the motor without transmission. The error propagation of a multiplication is given with [18]:

$$Q = ab \dots c, \quad (66)$$

$$\frac{\delta Q}{|Q|} = \sqrt{\left(\frac{\delta a}{a}\right)^2 + \left(\frac{\delta b}{b}\right)^2 + \dots + \left(\frac{\delta c}{c}\right)^2} \quad (67)$$

The perpendicularity between the attack angle of the force and the lever is expressed as  $\alpha$  and has equal influence on the applied force on the lever as the mass  $m$ . Thus they are expressed in one term. The propagation of uncertainty for the calculation of the transmission ratio results in:

$$\frac{\delta r}{r} = \sqrt{\left((1 - \cos \alpha) + \frac{\delta m}{m}\right)^2 + \left(\frac{\delta l}{l}\right)^2} \quad (68)$$

The used scale does not specify its precision so an high uncertainty of  $\pm 0,2 \text{ kg}$  is estimated which includes the reading accuracy of the scale. The accuracy of the perpendicularity is estimated to  $\pm 5^\circ$  as this can be visually verified during the test. For the force scale a grove inside the lever has to be filed in and an filing accuracy of  $\pm 2 \text{ mm}$  is estimated.

To get an overview of the possible uncertainties the following table shows resulting errors for different masses at a lever length of 100 mm.

Mass	Transmission ratio	relative Error	absolute Error
3 kg	9,3	7,3%	0,7
6 kg	18,9	4,2%	0,8
9 kg	27,9	3,3%	0,9

Table 39: Propagation of uncertainty

From equation (68) it can be seen that the error is inversely proportional to the mass and the leverage. To increase the mass while maintaining the torque the leverage has to be shortened and the relative error stays about the same. It is noticed, that the motor skips steps after roughly  $15^\circ$  even when no load is applied. This can be caused by the heat increase and the corresponding increase of coil resistance which would require more current than is supplied. To bypass this problem it is calculated, that the expected force for the transmission is achieved in less than  $15^\circ$ . A lever length of 100 mm is used for the transmission ratio calculation with the force scale.

#### 6.4 Transmission Tests

The resulting transmission ratio for each design is tested in two different test setups. The first setup was similar to chapter 6.1, but instead of being mounted to a fixed frame via the specimen, the lever is either attached to the motor (motor torque test) or at the end of the transmission (transmission ratio test). At the end of the lever, a defined mass is attached. The motor spins in an anticlockwise rotation and the angle at which the motor skips steps or the transmission slips is measured. Together with the gravitational force of the mass the occurring torque is deduced.

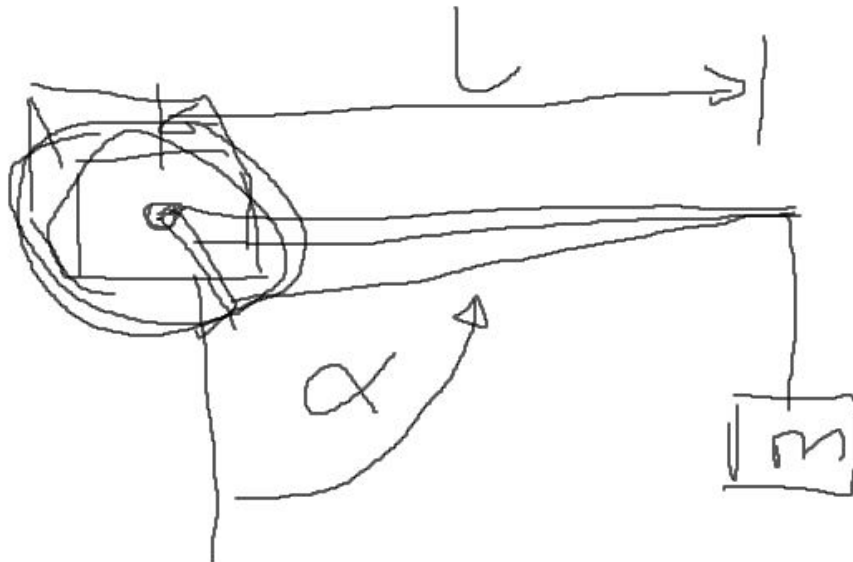


Figure 39: First test setup for the Torque and Transmission Test

To calculate the transmission ratio the actual torque of the motor with the applied controlling mechanism was tested with this setup.

Nr.	Mass [g]	Angle [°]	F [N]	Torque [Nm]	Torque Ave. [Nm]
1	50	60,0	0,4	0,11	
2	100	31,0	0,5	0,13	
3	130	26,0	0,6	0,15	
4	50	62,0	0,4	0,11	0,13
5	100	90,0	1,0	0,26	
6	130	72,0	1,2	0,32	
7	130	64,8	1,2	0,30	
8	130	86,4	1,3	0,33	0,32

Table 40: Torque Results of the Motor (17HS4401, ref. Appendix A)

As written in chapter 6.2 the first tests were conducted with a motherboard of a 3D with a current limitation below the required current of the motor. This resulted in the underperforming torque of 0,13 Nm. After the switch to the Stepper Shield a higher torque of 0,32 Nm was achieved. While still being less than the claimed torque of 0,42 Nm this control mechanism is used for further testing.

Table 41 shows the iteration process of the timing belt and the corresponding transmission ratios which were also tested with the first test setup. During the first design, the gears of the timing belt slipped inside the transmission. It could be seen that the *Rotating* part was deformed, causing a wider gap between the belt and the gears. A thicker wall and a larger *Wave Generator* resolved this problem. During the second test, the torque and the gap between the *Rotating* and the *Stationary* part caused a radial deformation of the timing belt, resulting in gears skipping. A reduced gap between the parts resulted in a higher transmission ratio of 7,9. The limiting factor was still a slipping of the timing belt. A larger *Wave Generator* with closer secondary bearings resulted in the highest achieved transmission ratio of 10,4.

Nr	Mass [g]	Angle [°]	F [N]	Torque [Nm]	r
1	575	80,0	5,6	1,45	4,6
2	840	75,0	8,0	2,08	6,6
3	840	90,0	8,2	2,15	6,8
4	1010	76,5	9,6	2,51	7,9
5	1010	45,0	7,0	1,83	5,8
6	1010	90,0	9,9	2,59	8,2
7	1050	90,0	10,3	2,69	8,5
8	1120	90,0	11,0	2,87	9,1
9	1250	90,0	12,3	3,20	10,1
10	1345	73,8	12,7	3,31	10,4

Table 41: Transmission Tests for the Timing Belt Design

The TPU design was tested with in the same test setup and it became clear, that the flex spline which was printed in TPU was not able to transmit the torque. Already at 600 g the flex spline deformed that much, that the wave generator was slipping. This underperformance of  $r = 1,9$  led to the neglection of this design.

Nr	Mass [kg]	F [N]	Torque [Nm]	r
1	0,6	5,9	0,59	1,9

Table 42: Transmission Test for the TPU Design

As written in chapter 5.1.3 the cycloidal design was investigated. A higher transmission ratio required a higher mass to conduct the tests. But at this point the mass could not be easily increased. A new test setup is made which included the force scale used in chapter 6.1 and the lever length was shortened to 100 mm as described in chapter 6.3. With this setup the targeted torque for the joints (chapter 4.8) could theoretically be achieved.

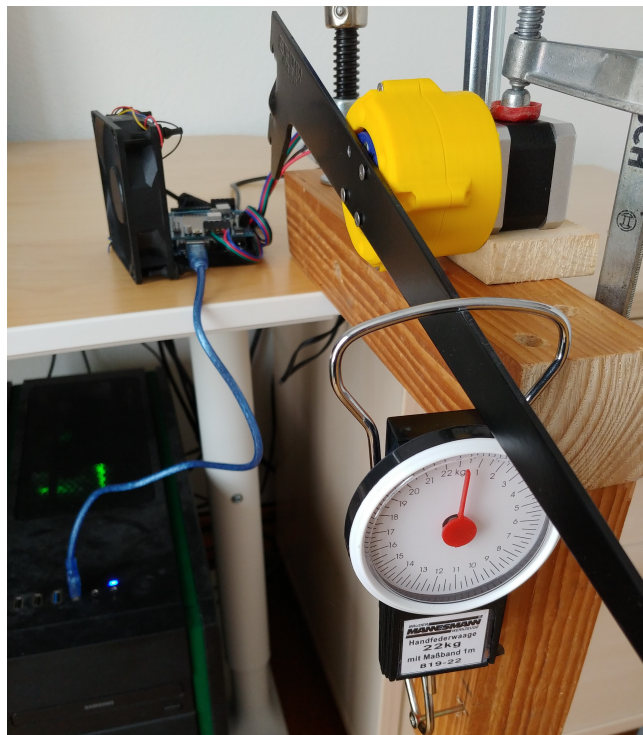


Figure 40: Adapted Torque Test setup

The first design used the theoretical transmission ratio of 30:1. After several iterations no major progress to further increase the effectivity could be made and the effectivity of 74% was seen well enough.

Nr	Mass [kg]	r	Error		Effectivity
			rel.	abs.	
1	4,1	12,8	5,6%	0,7	43%
2	3,0	9,3	7,3%	0,7	31%
3	3,0	9,3	7,3%	0,7	31%
4	6,2	19,1	4,1%	0,8	64%
5	5,0	15,5	4,8%	0,7	52%
6	4,8	14,9	5,0%	0,7	50%
7	6,1	18,8	4,2%	0,8	63%
8	7,1	22,1	3,8%	0,8	74%

Table 43: Transmission Tests for Cycloidal Drive (30:1)

A second design was made, which considered this effectivity and resulted in a theoretical transmission ratio of 43:1. The test confirmed the achievable effectivity and resulted in a final transmission ratio of 31:1:1.

Nr	Mass [kg]	r	Error		Effectivity
			rel.	abs.	
1	4,6	21,3	0,0	1,0	49%
2	7,7	23,8	0,0	0,8	55%
3	5,4	25,2	0,0	1,1	59%
4	9,0	28,0	0,0	0,8	65%
5	9,0	27,9	0,0	0,8	65%
6	9,1	28,2	0,0	0,8	66%
7	10,1	31,1	0,0	0,8	72%

Table 44: Transmission Tests for Cycloidal Drive (43:1)

Design	max. r	point of Failure
TPU	1,9	Flex Spline is too soft to transfer the required torque
PLA	-	PLA is too brittle when thin enough to flex
Timing Belt	10,4	Timing belt is too soft and deforms at higher loads
Cycloidal 30:1	22,1	74% effectivity
Cycloidal 43:1	31,1	72% effectivity

Table 45: Summary of design types

## 6.5 Transmission Selection

With this tests and the required transmission ratios, it was decided to use the 43:1 transmission for joint 2, the 30:1 transmission for link 1, 3 and 4 and that no transmission is required for joint 5. Joint 4 would not require a transmission as the gravitational force would always orient the last link in the right direction. If the ground is not level or the arm needs to be positioned very accurately a transmission is indeed beneficial. The removal of this transmission would only result in a moment reduction at joint 2 of 0,73 Nm and the added dexterity is considered more beneficial than the removed weight of the arm.

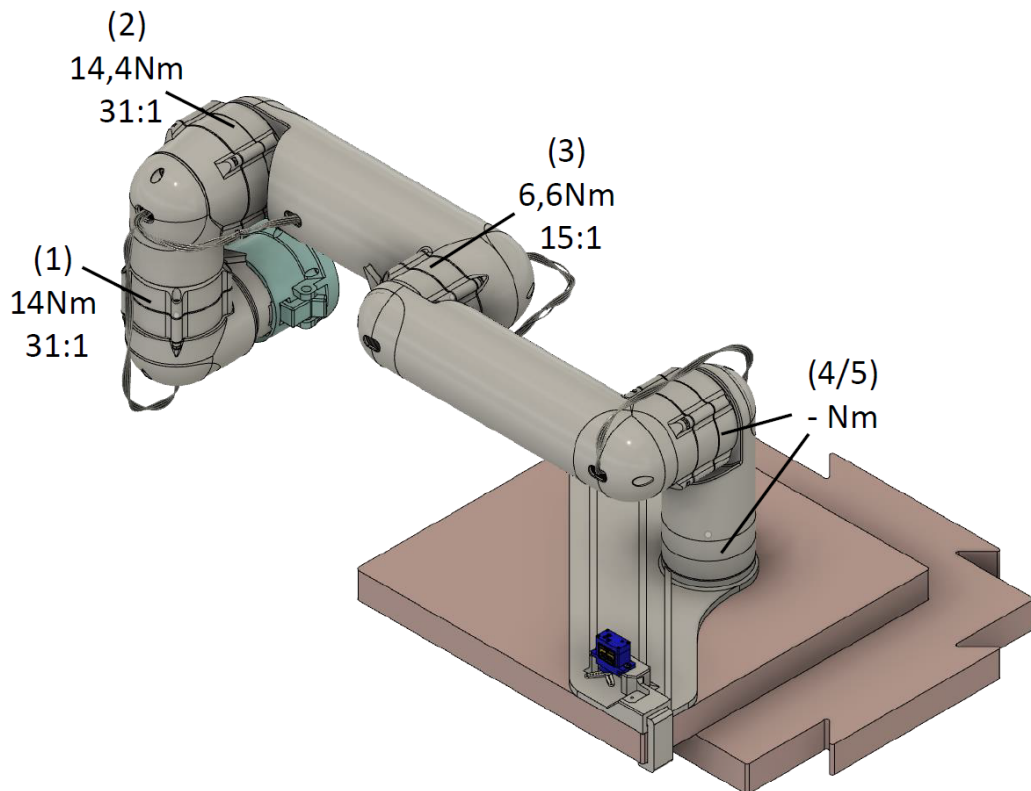


Figure 41: Required transmission ratios for each joint

## 7 Assembly

### 7.1 Assembly of the Cycloidal Drive

The parts needed for the assembly of the cycloidal drive for joint 2 are listed in Table 46.

Start by inserting the 12x28x7 bearings into the *Cycloidal Discs*. Insert the *Eccenter* and connect both cycloidal discs (Figure 42a).

Figure 42b is upside down. Insert the M3x25 through the *Output Shaft Middle* and place the *spacers* onto the screws and insert the nuts in this part as well. These slots are slightly undersized to prevent the nuts from dropping out during the assembly. Heating them will ease the inserting process. Next drop the cycloidal disc assembly onto the spacers. Make sure that the dots on the *cycloidal discs* are aligned.

Push the 35x47x7 bearing into the *Hull*. It should be a firm sit, otherwise use screws M3x16 screws, washer and nuts to fix the bearing in place. Insert the nuts into the *Output Shaft Upper* and place the assembly into the bearing (Figure 42c).

Screw the Lower Output Shaft assembly to the Upper output shaft assembly using M3x20 screws and then push this assembly into the *Frame*.

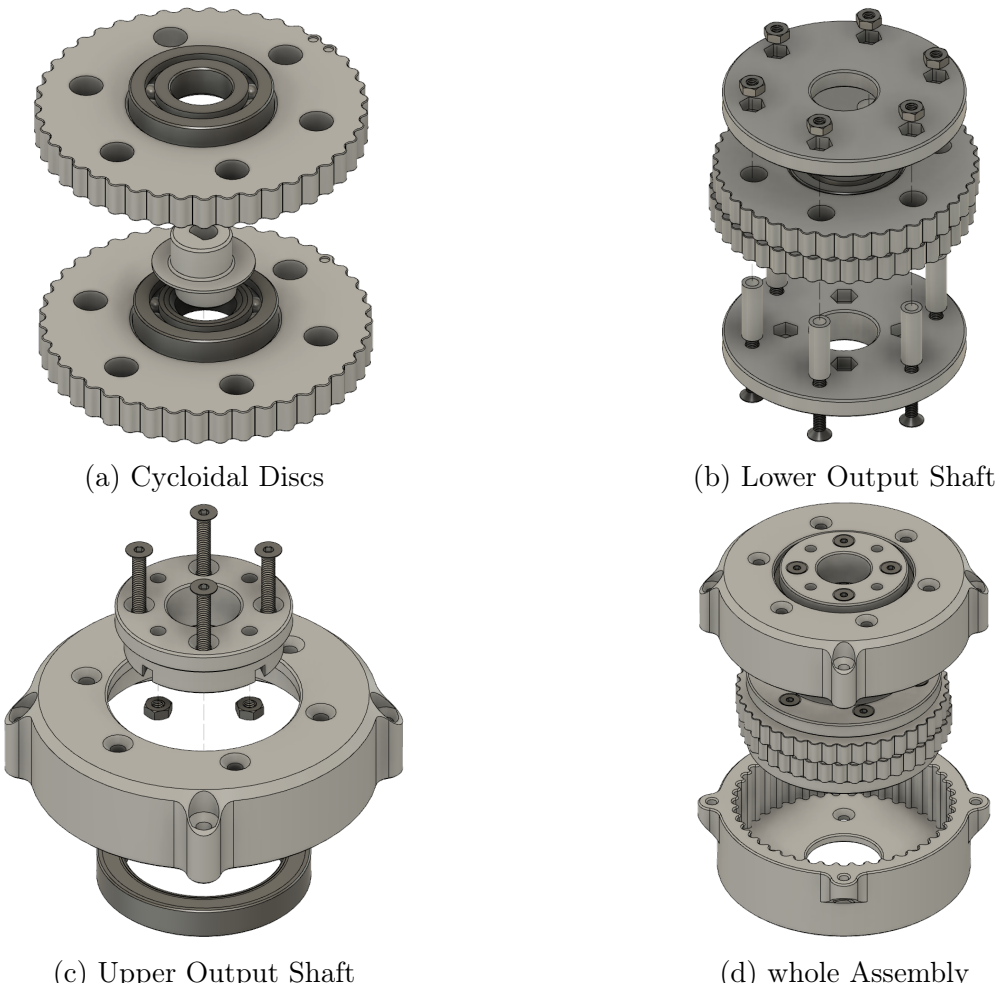


Figure 42: Cycloidal Drive Assembly

Item #	Part Name	Part Number	Make/Buy	Quantity	Material
1	Frame		Make	1	PLA
2	Nut - M3	90592A085	Buy	20	Steel
3	Screw - M3x25	91294A138	Buy	6	Steel
4	Screw - M3x20	91294A136	Buy	4	Steel
5	Screw - M3x16	91294A134	Buy	6	Steel
6	Washer - M3 8x0.7	95610A330	Buy	6	Steel
7	Cycloidal Disk		Make	1	PLA
8	Cycloidal Disk 2		Make	1	PLA
9	Output Shaft Lower		Make	1	PLA
10	Output Shaft Middle		Make	1	PLA
11	Output Shaft Upper		Make	1	PLA
12	Eccenter		Make	1	PLA
13	Spacer		Make	6	PLA
14	Bearing - 12x28x7	6455K179	Buy	2	Steel
15	Bearing - 5x16x5	6153K15	Buy	1	Steel
16	Bearing - 35x47x7	4648K234	Buy	1	Steel
17	Hull		Make	1	PLA

Table 46: Bill of Material for Cycloidal Drive (43:1)

## References

- [1] R. Kelso, R. Romo, C. Andersen, R. Mueller, Lippitt, N. Gelino, J. Smith, I. Townsend, J. Schuler, M. Nugent, A. Nick, K. Zacny, M. Hedlund, N. Gelino@nasa, J. Gov, Gov, M. Nugent@nasa and A. Gov, „Planetary Basalt Field Project: Construction of a Lunar Launch/Landing Pad, PISCES and NASA Kennedy Space Center Project Update“, Jan. 2018.
- [2] R. Volpe, T. Ohm, R. Petras, R. Welch, J. Balaram and R. Ivlev, „A prototype manipulation system for Mars rover science operations“, in *Proceedings of the 1997 IEEE/RSJ International Conference on Intelligent Robot and Systems. Innovative Robotics for Real-World Applications. IROS '97*, vol. 3, 1997, 1486–1492 vol.3.
- [3] E. T. Baumgartner, R. G. Bonitz, J. P. Melko, L. R. Shiraishi and P. Chris Leger, „The Mars Exploration Rover instrument positioning system“, in *2005 IEEE Aerospace Conference*, 2005, pp. 1–19.
- [4] R. Bonitz, L. Shiraishi, M. Robinson, J. Carsten, R. Volpe, A. Trebi-Ollennu, R. E. Arvidson, P. C. Chu, J. J. Wilson and K. R. Davis, „The Phoenix Mars Lander Robotic Arm“, in *2009 IEEE Aerospace conference*, 2009, pp. 1–12.
- [5] M. Robinson, C. Collins, P. Leger, W. Kim, J. Carsten, V. Tompkins, A. Trebi-Ollennu and B. Florow, „Test and validation of the Mars Science Laboratory Robotic Arm“, in *2013 8th International Conference on System of Systems Engineering*, 2013, pp. 184–189.
- [6] A. Rusconi, P. Magnani, T. Grasso, G. Rossi, J. Gonzales Lodoso and G. Magnani, „DEXARM - a Dextrous Robot Arm for Space Applications“, in *8th ESA Workshop on Advanced Space Technologies for Robotics and Automation Astra 2004*, 2004.
- [7] R. Jazar, „Theory of Applied Robotics: Kinematics, Dynamics, and Control“, 2007.
- [8] S. Buss, „Introduction to Inverse Kinematics with Jacobian Transpose , Pseudoinverse and Damped Least Squares methods“, Oct. 2009.
- [9] V. Iliukhin, K. Mitkovskii, D. Bizyanova and A. Akopyan, „The Modeling of Inverse Kinematics for 5 DOF Manipulator“, *Procedia Engineering*, vol. 176, pp. 498–505, 2017.
- [10] L.-W. Tsai, *Robot Analysis and Design: The Mechanics of Serial and Parallel Manipulators*, 1st. USA: John Wiley & Sons, Inc., 1999, ISBN: 0471325937.
- [11] SD3D. (Feb. 2021). PLA Technical Data Sheet, [Online]. Available: [https://www.sd3d.com/wp-content/uploads/2017/06/MaterialTDS-PLA\\_01.pdf](https://www.sd3d.com/wp-content/uploads/2017/06/MaterialTDS-PLA_01.pdf). (accessed: 25.02.2021).

- [12] G. Czerwenka and W. Schnell, *Einführung in die Rechenmethoden des Leichtbaus II*. Hochschultaschenbücher Verlag, 1970.
- [13] Harmonic Drive SE. (2021). Harmonic Drive Strain Wave Gear, [Online]. Available: <https://harmonicdrive.de/en/technology/harmonic-drive-strain-wave-gears>. (accessed: 28.01.2021).
- [14] Dejan. (2020). What is Strain Wave Gear a.k.a Harmonic Drive? A Perfect Gear Set For Robotics Applications!?, [Online]. Available: <https://howtomechatronics.com/how-it-works/what-is-strain-wave-gear-harmonic-drive-a-perfect-gear-set-for-robotics-applications/>. (accessed: 25.11.2020).
- [15] Simon Merret. (2020). Strain Wave Gear with Timing Belts, [Online]. Available: <https://hackaday.io/project/19405-strain-wave-gear-with-timing-belts>. (accessed: 25.11.2020).
- [16] Stepperonline. (2020). Stepper Motor & Stepper Motor Drivers, [Online]. Available: <https://www.omc-stepperonline.com/>. (accessed: 25.11.2020).
- [17] Tec - Science. (Jan. 2019). Construction of the cycloidal disc, [Online]. Available: <https://www.tec-science.com/mechanical-power-transmission/cycloidal-drive-speed-reducer-gear/construction-of-the-cycloidal-disc/>. (accessed: 28.01.2021).
- [18] Instructional Physics Laboratory. (2013). A Summary of Error Propagation, [Online]. Available: [http://ipl.physics.harvard.edu/wp-uploads/2013/03/PS3\\_Error\\_Propagation\\_sp13.pdf](http://ipl.physics.harvard.edu/wp-uploads/2013/03/PS3_Error_Propagation_sp13.pdf). (accessed: 20.01.2021).

# A Usongshine - 17HS4401

16.12.2020 1pcs 17HS4401 Conventional V5 V6 4 lead Nema17 Stepper Motor 42 motor Nema 17 motor 42BYGH 1.5A (17HS4401) motor for CNC|nema 17 motor|nema17 stepper motorstepper motor 42 - AliExp...

**Usongshine Store**

- Store Categories**
  - CNC Engraving machine
  - CNC engraving machine
  - Nema Stepper Motor
    - Nema 17
    - Nema 23
    - Stepper Motor Driver
  - Other Accessories
    - DIY Kit
    - Drag Chain
    - Switch
    - other
  - 3D printer Accessories 2
    - Timing belt
    - Synchronous wheel
    - Coupling
    - Idler Timing Pulley
    - Screw
    - Polished--rod
    - Linear Guides 3D printer
    - mini cooling fan
    - Linear bearing
  - Bearing
    - Bearing steel pulley
  - 3D printer Accessories 1
    - Extruder
    - nozzle
    - Aluminum block
    - Throat
    - spring
    - copper column
    - Nut
    - Linear guide slider
  - Others

**OVERVIEW** CUSTOMER REVIEWS (4) SPECIFICATIONS

Usongshine Store  
97.6% Positive Feedback  
1811 Followers  
Contact

+ Follow Visit Store

€ 21,54 € 22,04 € 7,15 € 21,81 € 22,92 € 21,81

**OVERVIEW** CUSTOMER REVIEWS (4) SPECIFICATIONS

1pcs 17HS4401 Conventional V5 V6 4-lead Nema17 Stepper Motor 42 motor Nema 17 motor 42BYGH 1.5A (17HS4401) motor for CNC

Package: 17HS4401 with 1 meter wire

17hs4401 stepper motor			
Feature	Specification	Feature	specification
Phase	2	Step Angle(degrees)	1.8°±0.09°
Rated Voltage	DC 3.6V	Rated Current	DC 1.5A/Phase
Phase Resistance(20°C)	2.4*(1±15%)Ω/Phase	Phase Inductance	3.7*(1±20%)mH/Phase
Holding Torque	≥420mN.m	Positioning Torque	15 mN.m REF.
Rotating direction	A-AB-B Clockwise	Maximum starting rate	≥1500 PPS
Maximum slewing rate	≥1900 PPS	Insulation resistance	≥100 MΩ (DC 500V)
Electrical strength	AC600V/1mA/1S	Insulation class	B

<https://www.aliexpress.com/item/32822607212.html?spm=2114.12010612.8148356.19.255b22b0HgFhJi>

2/19

16.12.2020 1pcs 17HS4401 Conventional V5 V6 4 lead Nema17 Stepper Motor 42 motor Nema 17 motor 42BYGH 1.5A (17HS4401) motor for CNC|nema 17 motor|nema17 stepper motorstepper motor 42 - AliExp...

**Usongshine Store**

- OVERVIEW** CUSTOMER REVIEWS (4) SPECIFICATIONS

**USONGSHINE**  
€ 0,55 ★ 4.9 166 Sold

**USONGSHINE 17HS4401/17HS4401**  
€ 21,81 ★ 4.8 99 Sold

**USONGSHINE**  
5PCS 17HS4401  
€ 21,54 ★ 4.9 175 Sold

**OVERVIEW**

Unmarked tolerances according to IT14

Basic parameters/mm	Tolerance value
0-3	0.25
3-6	0.3
6-10	0.36
10-18	0.43
18-30	0.52

**Electrical principle**

<https://www.aliexpress.com/item/32822607212.html?spm=2114.12010612.8148356.19.255b22b0HgFhJi>

3/19

# B Bearing - 61807



Erstellt von www.skf.com am 2021-02-22



## 61807

Beliebtes Produkt

### Rillenkugellager

Lagerdaten

[Toleranzen:](#)

Normal (metrisch), P6, P5, Normal  
(Zoll),

[Radialluft:](#)

Zusammengesetzte Lagerpaare,  
Nichtrostender Stahl  $d < 10$  mm,  
Sonstige Lager

Gestaltung der

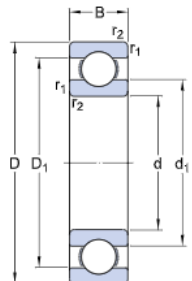
Lagerumbauteile

[Passungsempfehlungen,](#)

Toleranzen und Passung

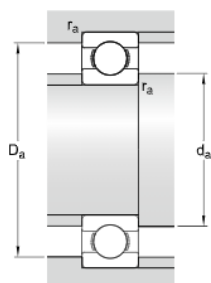
### Technische Spezifikationen

#### ABMESSUNGEN



d	35 mm
D	47 mm
B	7 mm
d <sub>1</sub>	≈ 38.21 mm
D <sub>1</sub>	≈ 42.75 mm
r <sub>1,2</sub>	min. 0.3 mm

#### ANSCHLUSSMASSE



d <sub>a</sub>	min. 37 mm
D <sub>a</sub>	max. 45 mm
r <sub>a</sub>	max. 0.3 mm



Seite 1 von 3

# B Bearing - 61807



Erstellt von www.skf.com am 2021-02-22

## BERECHNUNGSDATEN

Dynamische Tragzahl	C	4.36 kN
Statische Tragzahl	$C_0$	3.35 kN
Ermüdungsgrenzbelastung	$P_u$	0.14 kN
Referenzdrehzahl		30 000 r/min
Grenzdrehzahl		18 000 r/min
Berechnungsfaktor	$k_r$	0.015
Berechnungsfaktor	$f_0$	14.3

## GEWICHT

Gewicht Lager	0.029 kg
---------------	----------

## Weitere Informationen

Produktdetails	Konstruktionsinformationen	Werkzeuge
<a href="#">Einreihige Rillenkugellager</a>	<a href="#">Entwurf von Lagerungen</a>	<a href="#">Bearing Select</a>
<a href="#">Einreihige Rillenkugellager aus nichtrostendem Stahl</a>	<a href="#">Allgemeines Lagerwissen</a>	<a href="#">SimPro Quick</a>
<a href="#">Einreihige Rillenkugellager mit Einfüllnuten</a>	<a href="#">Lagerauswahlprozess</a>	<a href="#">Engineering Calculator</a>
<a href="#">Zweireihige Rillenkugellager</a>	<a href="#">Gestaltung der Lagerumbauteile</a>	<a href="#">LubeSelect für SKF Schmierfette</a>
<a href="#">Lagerdaten</a>	<a href="#">Passungsempfehlungen</a>	<a href="#">Hilfsmittel zur Auswahl von Anwärmgeräten</a>
<a href="#">Belastungen</a>	<a href="#">Wahl der Lagerluft</a>	<a href="#">Ein- und Ausbauanleitung für Wälzlager</a>
<a href="#">Temperaturgrenzwerte</a>	<a href="#">Schmierung</a>	
<a href="#">Zulässige Drehzahlen</a>	<a href="#">Abdichtung, Ein- und Ausbau</a>	
<a href="#">Bezeichnungsschema</a>	<a href="#">Lagerausfall und wie Sie ihn verhindern</a>	



Seite 2 von 3